Using MRI to Investigate the Effect of Brain Iron in Neurodegerative Disease

by Winona Barnett, MSci (Hons)

Thesis submitted to the University of Nottingham for the degree of Master of Research, November 2019.

Acknowledgments

I would like to thank Professor Richard Bowtell and Dr Olivier Mougin. Thank you for supporting and encouraging me throughout my time at SPMIC.

Table of Contents

Abstract

This work was focused on designing a model which could simulate the gradient echo signal evolution when spins experience spatially varying magnetic fields due to the presence of spherical particles of different magnetic susceptibility. The cases where the spins are stationary and when they undergo diffusion have both been considered. The model initially was designed to look at the effect of a singular stationary sphere with a volume magnetic susceptibility of $1x10^{-6}$ in a magnetic field of 7T. It was seen that the average frequency offset and rate of signal decay scaled with the volume fraction occupied by the sphere, in accordance to the literature. The model was then modified with a random walk algorithm. The displacement of the particles after a given time was assessed by looking at the standard deviation, σ, after each time step. A plot of σ^2 against time was created and a positive linear relationship was seen between the two variables. The model was then used to simulate 10,000 perturbers moving in a magnetic field. A mono-exponential signal decay was observed and increasing the diffusion step size decreased R_2* and the frequency offset.

Three patients who suffer from Alzheimer's disease (AD) were scanned on a Philips 7T Achieva MRI scanner and a T_2* and GRE scan was carried out using a Nova 2Tx/32Rx coil with TE=20 ms. Quantitative susceptibility maps were created from the resulting data in order to look at the feasibility of measuring the susceptibility in the hippocampus in AD patients in a larger study.

Outline

Chapter one provides background information relating to magnetic resonance, quantitative susceptibility mapping, static dephasing regimes, diffusion effects in MRI, and iron storage in the brain. The motivation for this work is also discussed in this chapter.

Chapter two focuses on the computer simulations which were carried out in order to investigate the static dephasing regime and how diffusion can cause changes in the evolution of the magnetic resonance signal's phase and magnitude in the presence of regions of different magnetic susceptibility. The first section in this chapter describes the use of MATLAB R2018a (Mathworks, MA, USA) to model the effect on the NMR signal of a single stationary sphere and a distribution of spherical inclusions of different magnetic susceptibility exposed to uniform polarising field. The results are compared to those expected in the static dephasing regime (1). The second section adapts the previously created model by developing a random walk algorithm which is then used to model the effect on the NMR signal of diffusion of water in the magnetic field distribution around a random distribution of spherical inclusions of different magnetic susceptibility. Signal and phase data are analysed and relaxation times for various magnetic susceptibilities and rates of diffusion are compared.

Chapter three investigates how quantitative susceptibility mapping can be used to image the hippocampus in healthy individuals and in individuals who suffer from Alzheimer's disease.

Chapter four summarises the findings of this thesis and discusses conclusions and the potential for future work.

List of Abbreviations

AD	Alzheimer's Disease
ASL	Arterial Spin Labelling
BBB	Blood Brain Barrier
CN	Caudate Nucleus
CSF	Cerebral Spinal Fluid
FID	Free Induction Decay
GE	Gradient Echo
GP	Globus Pallidus
GM	Grey Matter
LC	Locus Coeruleus
MRI	Magnetic Resonance Imaging
MSDI	Multi-Scale Dipole Inversion
MPTP	(1-methyl-4-phenyl-1,2,3,6-tetrahydropyridine)
NM	Neuromelanin
PD	Parkinson's Disease
PUT	Putamen
QSM	Quantitative Susceptibility Mapping
RN	Red Nucleus
rms	Root Mean Squared
RF	Radio Frequency
SMV	Spherical Mean Value
SN	Substantia Nigra
SNc	Substantia Nigra Pars Compacta
TfR	Transferrin Receptor
TH	Thalamus
WM	White Matter

List of Symbols

B_0	Static magnetic field strength in T
B_Z	Spatially varying magnetic field strength in T
B_{NMS}	Magnetic induction field in T
ΔB_{inhom}	Field inhomogeneity across voxels in T
D	Diffusion coefficient in $m^2 \cdot s^{-1}$
H^L	Depolarising magnetic moment in $A \cdot m^{-1}$
H^E	Shimming residual in $A \cdot m^{-1}$
H_0	Applied magnetic field in $A \cdot m^{-1}$
$\hbar$	Reduced Planck's constant equal to 1.055 $x10^{-34}$ J.s
J	Spin angular momentum in $kg \cdot m^2\ s^{-1}$
M	Magnetisation vector in $A \cdot m^{-1}$
M_0	Bulk magnetisation in $A \cdot m^{-1}$
M_t	Magnetisation after time t in $A \cdot m^{-1}$
M_{max}	Maximum magnetisation in $A \cdot m^{-1}$
n	Population difference in a.u
N	Total number of nuclei in a system in a.u
r	Radius of sphere (dipole) in µm
Δr	Voxel size in a.u
S	Spin quantum number in a.u
t_p	Duration of RF pulse in s
Δt	Timestep in s
TE	Echo time in s
T	Temperature in K
T_1	Spin lattice relaxation time in s
T_2	Spin-spin relaxation time in s
Z	Vertical dimension of the spherical space for the dipole field in a.u
v	Volume of object in µm

V	Volume of system in µm
VF	Volume fraction in a.u
γ	Gyromagnetic ratio in rad·s^{-1}·T^{-1}
θ	Angle from main magnetic field direction in rads
μ_0	Magnetic permeability of free space H.m^{-1}
µ	Magnetic moment in A·m^2
ρ	Coefficient which varies depending on scan parameters such as the sensitivity of hardware, flip angle and spin density.
ς	Volume fraction in a.u
σ	Standard deviation
τ	Time after magnetic field is applied (echo time) in s
τ_D	Diffusion time in s
ϕ	Phase in radians
χ	Volume magnetic susceptibility in a.u

1. Introduction

Contents

This chapter outlines the motivation behind this thesis and will provides necessary background information about magnetic resonance imaging, quantitative susceptibility mapping, and the role of iron in the brain.

1.1. Motivation

According to Alzheimer's Research UK in 2018 there were 850,000 people suffering from a form of dementia in the UK (2) and in America 10% of population who are over 65 also have this disease (3).

In England, AD and PD are normally diagnosed by a verbal exam and blood tests. Once symptoms of memory loss have been evaluated by a GP the patient is referred to a neurologist and a memory clinic. Currently no physical test is used in the UK to identify the condition. Structural MRI scans are sometimes carried out during the diagnosis of AD and PD with the purpose of eliminating other issues which cause similar symptoms (4). If relatively quick MR scans which produced reliable results were developed and could show the progression of AD, these could be integrated into the standard scans carried out on patients who are at risk. This would allow more time to organise financial, legal and healthcare plans for the future. It can take several months before a diagnosis can be reached as a result of there being a lack of any physical tests, ultimately causing a lot of distress for both patients and families alike.

Computer simulations are a very useful tool when investigating phenomena which aren't easily viewed and cannot be immediately examined in vivo. Patients who suffer from mild to moderate cognitive impairment due to AD may find being inside an MRI scanner for extended periods of time distressing. Performing MRI scans for research purposes often takes significantly longer than a standard hospital scan due to the need to undergo several different scans in order to establish a large data pool and to improve and develop scanning techniques. The time that the patient is kept in the scanner is always kept to a minimum and so computer simulations become important to help model potential outcomes in order to give other researchers the means to plan their future experiments efficiently.

1.2. Background

The following section will provide the necessary background knowledge in order to understand the work in this thesis.

1.2.1. Magnetic Resonance Imaging

Magnetic resonance imaging (MRI) is an imaging technique in which nuclear spins interact with an external magnetic field.

The spin angular momentum, **J**, of a nucleus can be defined by the equation 1:

$$|\mathbf{J}| = \hbar\sqrt{S(S+1).} \qquad [1]$$

where ħ is the reduced Planck's constant and S is the spin of the nucleus. Nuclear spin is quantised into integer and half-integer values e.g. *S*= 0, $^{1}/_{2}$, 1, $^{3}/_{2}$, 2.

Hydrogen nuclei are abundant in the human body as they make up part of lipids and water. These protons have spins with a value of *S*=$^{1}/_{2}$ and therefore have non-zero angular momentum (5).

A magnetic moment is associated to nuclei with non-zero spin and is given by equation 2.

$$\boldsymbol{\mu} = \gamma\mathbf{J}. \qquad [2]$$

In the presence of a magnetic field, B_0, the magnetic moment will align along a parallel component of $\overrightarrow{B_0}$ and experience a torque, causing the magnetic moment to precess around the magnetic field at an angle, θ (6, 7, 8). The angular momentum will change over time due to the precession shown by figure 1 and equation 3.

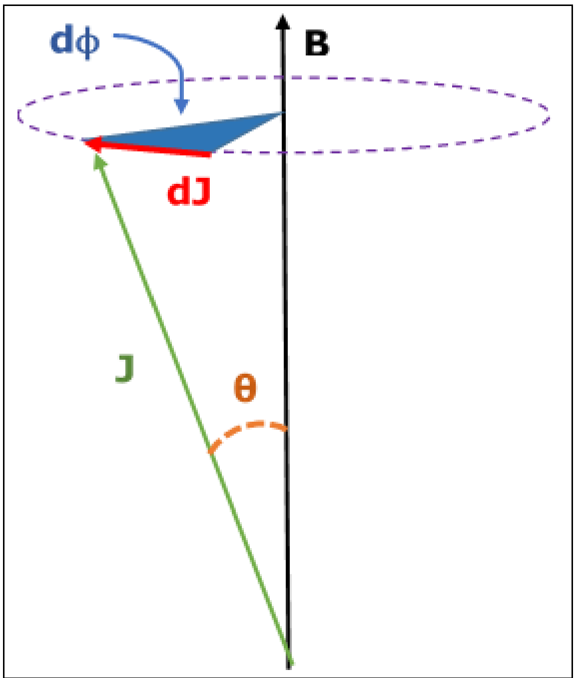

Figure 1. *Visual representation of angular momentum, J, precessing around magnetic field, B.*

$$\left|\frac{d\mathbf{J}}{dt}\right| = |\boldsymbol{\mu} \times \mathbf{B}| = |\gamma\mathbf{J} \times \mathbf{B}| = \gamma J B sin\theta. \qquad [3]$$

The frequency at which the momentum precesses around the field can be found by considering *d***J**:

$$d\mathbf{J} = Jsin\theta d\phi. \qquad [4]$$

The precessional frequency, ω, can be calculated by combining equations 3 and 4:

$$\omega = \frac{d\phi}{dt} = -\frac{d\phi}{d\mathbf{J}} \cdot \frac{d\mathbf{J}}{dt} = -\frac{\gamma J B sin\theta}{J sin\theta}. \qquad [5]$$

This results in the Larmor frequency, ω_0, which varies for each type of nucleus due to varying gyromagnetic ratios.

$$\omega = -\gamma|\mathbf{B}|, \quad [6]$$

Hence in the presence of a magnetic field of magnitude B_0 the Larmor frequency is given by

$$\omega_0 = \gamma\mathbf{B}_0. \quad [7]$$

The minus sign in equation 6 indicates a clockwise rotation about the axis.

The approach above used simple mechanics to find the Larmor frequency. The problem can also be solved by considering quantum mechanics. As stated in equation 2, spin angular momentum is quantised due to the spin of the protons also being quantised. Protons can only have two possible states when exposed to a magnetic field, corresponding to the components of the spin angular momentum along the field direction being given by $J = \pm\,{}^{\hbar}/_{2}$. The associated energy of each state is given by equation 8 when the field is applied in the z direction.

$$E = -\mu_z \cdot B_0. \qquad [8]$$

The separation of the two spin states is known as Zeeman splitting and results in an energy difference between the two states which is calculated as:

$$\Delta E = \left(\frac{1}{2} - -\frac{1}{2}\right)\mu_z B_0 = \gamma\hbar B_0. \qquad [9]$$

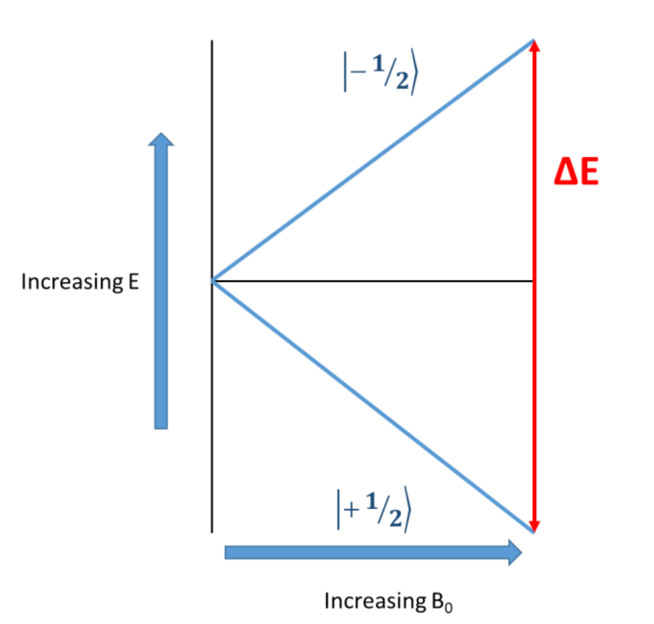

Figure 2. *A diagram showing Zeeman splitting. The two spin states are separated by an energy ΔE when exposed to an external magnetic field, B_0.*

The energy is associated with a frequency:

$$\Delta E = \hbar\omega_0. \qquad [10]$$

The precessional frequency, ω_0, can now be defined by combining the two previous equations:

$$\hbar\omega_0 = \gamma\hbar B_0, \qquad [11]$$

$$\omega_0 = \gamma B_0. \qquad [12]$$

The human body has an abundance of protons, as the body is 75% water (5). In this case, the bulk magnetisation, *M*, of the material should be considered by taking into account the population of protons in each energy state. The protons will either have a spin up or a spin down configuration when in a magnetic field, and for a large number of protons, the Boltzmann distribution gives the ratio of the number of protons in each energy state at temperature T as:

$$\frac{N_{up}}{N_{down}} = \exp\left(-\frac{\Delta E}{k_B T}\right), \quad [13]$$

where k_B is the Boltzmann constant.

The high temperature approximation can be used as body temperature as $\gamma\hbar B_0 << k_B T$ and the population difference, n, per unit volume can now be written:

$$n = N\left(\frac{\gamma\hbar B_0}{2k_B T}\right), \qquad [14]$$

where N is the total number of nuclei in the system. The bulk magnetisation parallel to the field, M_0, is the net magnetisation of the protons in each energy state and is given by:

$$M_0 = \frac{\gamma\hbar}{2}N_{up} - \frac{\gamma\hbar}{2}N_{down} \approx N\left(\frac{(\gamma\hbar)^2 B_0}{4k_B T}\right), \qquad [15]$$

in the high temperature limit where $k_B T \gg \hbar\omega_0$.

In higher magnetic fields, a larger amount of protons are aligned parallel to the field as bulk magnetisation is directly proportional to field strength. This will ultimately result in a higher signal to noise ratio at higher field strengths as more spins will be tipped once an RF pulse is applied, creating a larger measured signal.

A radio frequency (RF) pulse is applied at the Larmor frequency creating a rotating magnetic field, B_1, which is static when viewed in a rotating reference frame that also rotates at a frequency ω. The RF pulse tips M_0 from the z axis towards the x' axis (x' describes the x-axis in a rotating reference frame). The angle through which M_0 is tipped by is called the flip angle and is described by equation 16.

$$\alpha = \gamma B_1 t_p, \quad [16]$$

where t_p is the duration of the RF pulse. The subsequent precession of M in the transverse plane induces a voltage in the receiver coils of the MRI scanner and this signal, referred to as the free induction decay (FID), is recorded.

The Bloch equations describe the change in magnetisation due to the excitation and relaxation. Initially ignoring the effect of relaxation the change of magnetisation over time can be described by:

$$\frac{d\mathbf{M}}{dt} = \gamma\mathbf{M}\times\mathbf{B} = \gamma\begin{bmatrix}(M_y B_z - M_z B_y)\mathbf{i} \\ +(M_z B_x - M_x B_z)\mathbf{j} \\ +\left(M_x B_y - M_y B_x\right)\mathbf{k}\end{bmatrix}. \quad [17]$$

Relaxation occurs due to two mechanisms; spin-spin relaxation and spin lattice relaxation and the time constants for these processes are labelled T_1 and T_2 respectively. Taking relaxation into account, the evolution of the components of the magnetization is described by:

$$\frac{dM_x}{dt} = \gamma\left(M_y B_0 + M_z B_1 \sin(\omega t)\right) - \frac{M_x}{T_2}, \qquad [18]$$

$$\frac{dM_y}{dt} = \gamma(M_x B_1 \cos(\omega t) - M_x B_o) - \frac{M_y}{T_2}, \qquad [19]$$

$$\frac{dM_z}{dt} = \gamma\left(M_x B_1 \sin(\omega t) + M_y B_1 \cos(\omega t)\right) - \frac{M_z - M_0}{T_1}. \qquad [20]$$

The subscripts x, y and z in equations 17-20 refer to the magnetization in the x, y and z directions respectively. The magnetic field B_1 will be zero immediately after the RF field has been terminated and assuming the system was in a state of equilibrium before the RF was applied and that a 90° RF pulse rotated the equilibrium magnetisation to alignment with the x'-axis the above equations can be solved to give the magnetisations.

$$M_{xy}(t) = M_0 \exp(i\omega_0 t) \cdot \exp\left(\frac{-t}{T_2}\right), \quad [21]$$

$$M_z(t) = M_0 \left[1 - \exp\left(\frac{-t}{T_1}\right)\right]. \quad [22]$$

After the RF pulse has tipped the magnetisation into the transverse plane the individual spin contributions are in phase, resulting in a maximum of the magnetisation vector. Over time these spins will start to dephase and relax due to interactions with other spins, resulting in a loss of received signal. The time for the signal to be reduced by a factor of 1/*e* is called the transverse or spin-spin relaxation time, T_2 (5, 9). T_2* describes the time taken for a similar reduction in transverse magnetisation when dephasing of the spins also occurs due to the effects of field inhomogeneity, ΔB_{inhom}, and T_2* is always shorter than T_2. The inhomogeneity in the field can be caused by spatial encoding gradients and differences in magnetic susceptibilities of tissues (9). By applying a 180° pulse the dephasing can be refocused, however in gradient echo sequences the refocusing 180° pulse is absent. The relationship between T_2 and T_2* can be approximately described by the following equation:

$$\frac{1}{T_2{}^*} = \frac{1}{T_2} + \gamma \Delta B_{inhom}. \quad [23]$$

Signal is measured as a function of time, and the signal lost after an echo time, TE, is given by the relationship:

$$S(TE) \propto \exp(-R_2{}^* \cdot TE), \qquad [24]$$

$$R_2{}^* = \frac{1}{T_2} + R_2{}', \qquad [25]$$

where R_2' is the relaxation rate due to field homogeneities:

$$R_2{}' = \gamma \Delta B. \qquad [26]$$

The spin-lattice relaxation time, T_1, describes the time taken for the component of the magnetisation along B_0 to recover to its equilibrium value. The relaxation of nuclei from their excited state to their ground state is a result of interactions with surrounding nuclei (10, 11). The magnetisation vector recovers exponentially over time after a 90° RF pulse. T_1 weighted imaging is useful for imaging parts of the body where a high contrast is needed between areas with high water content and fatty tissues, and where paramagnetic contrast agents, such as gadolinium, have been used (12).

1.2.2. K-Space

MRI data is not collected in the spatial domain, instead it is collected in the spatial frequency domain, generally known as k-space. The scan data is stored as an array of values corresponding to the amplitudes of the spatial frequencies that characterise the object being imaged. . Considering a two-dimensional object, the measured signal is expressed by equation 27.

$$S(k_x, k_y) = \iint \rho(x, y) e^{-i2\pi(k_x x + k_y y)} dxdy, \quad [27]$$

where $S(k_x, k_y)$ is the frequency signal intensity of the k-space point ($k_x\, k_y$) and $\rho(x, y)$ is the spin density, which characterises, the concentration of hydrogen nuclei at spatial position (x,y).

To obtain spin density measurements from the k-space data, an inverse Fourier transform must be performed:

$$\rho(x, y) = \iint S(k_x, k_y) e^{-i2\pi(k_x x + k_y y)} dk_x dk_y \qquad [28]$$

In reality these measurements are taken over a finite region of k-space and so there are discrete Fourier transforms for each voxel in an image. The spatial resolution of an image is related to the extent of k-space that is spanned by the measurements (13).

1.2.3. Quantitative Susceptibility Mapping

The total net magnetisation of a material, which dominated by the effect of the electrons rather than the nuclei, can be described by a magnetisation vector, **M**, described in equation 29.

$$\mathbf{M} = \chi\mathbf{H}. \qquad [29]$$

Volume magnetic susceptibility, χ, is a dimensionless proportionality constant which describes the degree that an applied magnetic field, **H**, effects the bulk magnetisation of the material (14). Materials can be organised into categories by their magnetic susceptibility; paramagnetic ($\chi>0$), diamagnetic ($\chi<0$) and ferromagnetic ($\chi>>0$).

Most materials in the human body are slightly diamagnetic, and have an overall magnetisation of zero in the absence of an external magnetic field (14). Electrons orbit around the nucleus in strictly defined orbitals creating current loops. When an external magnetic field is applied, the orbitals are altered by interaction with the field, producing an additional magnetic field. The field which is induced in the material is always in an opposite direction to the applied external field, resulting in a negative susceptibility (6, 14).

Paramagnetic materials contain unpaired electrons resulting in the constituent having atoms with a non-zero magnetic moment (14, 15). When exposed to a magnetic field, the magnetic moments partially align along the direction of the applied field. Atoms which have non-zero magnetic moments make a positive contribution to the overall susceptibility of a material. Iron, cobalt and nickel are examples of paramagnetic atoms.

When material with non-zero magnetic susceptibility is placed in the strong uniform magnetic field of an MRI scanner, $\mathbf{B} = B_0\,\mathbf{k}$, magnetisation M_z is induced in it and this magnetisation generates a small perturbing magnetic field ΔB_z whose magnitude can be measured from the phase of a gradient echo signal in MRI.

Quantitative susceptibility mapping is a method of analysing phase data obtained from gradient echo (GE) MRI scans to produce information which describes the magnetic susceptibility of tissues (16). Phase data is useful in quantitative analysis as it depends on variations in local magnetic fields. Phase, $\emptyset$, can be related to precessional frequency, ω, and time, t, by equation 30:

$$\omega = \frac{d\phi}{dt}, \qquad [30]$$

The main source of phase contrast in the brain is caused by the presence of iron (17). The phase of the signal produced by a gradient echo sequence with an echo time, TE, is given by equation 31 (17).

$$\phi(\vec{r}) = \phi_0(\vec{r}) + \gamma\Delta B_z(\vec{r})TE, \quad [31]$$

where $\phi_0(\vec{r})$ is the phase offset due to the coil sensitivity and other instrumental effects, and ΔB_z is the z component of the field variation. ΔB_z, can be found by using the convolution of the magnetization, $M_z(\vec{r})$, and the point dipole response $D(\vec{r})$ as seen in equation 32 (17).

$$\Delta B_z(\vec{r}) = \mu_0 M_z(\vec{r}) * D(\vec{r}) \quad [32]$$

where

$$D(\vec{r}) = \left(\frac{3z^2/_{r^2}-1}{r^3}\right), \qquad [33]$$

is the characteristic dipolar field of a unit dipole.

MRI data is collected in k-space and is then inverse Fourier transformed to provide images we can view in a spatial domain. With this in mind, $D(\vec{r})$ can also be transformed into k-space to produce $D(\vec{k})$ and $\Delta B_z(\vec{r})$ and can then be related to the magnetic susceptibility using equation 34.

$$\Delta B_z(\vec{r}) = B_0 \cdot FT^{-1}\{\chi(\vec{k}) \cdot D(\vec{k})\}, \quad [34]$$

where $\chi(\vec{k})$ is the 3D Fourier transform of $\chi(\vec{r})$ and

$$D(\vec{k}) = \left(\frac{1}{3} - \frac{k_z^2}{|\vec{k}|^2}\right), \qquad [35]$$

It has been shown that ΔB_Z is sensitive to the magnetic susceptibility of the material being imaged. This results in a change in phase Δϕ, therefore by using a GE scan phase data can be obtained, and the difference in phase over areas of the image can be used to create a map of susceptibility (18).

A review article about QSM written by E.M. Haacke *et al*. demonstrated the type of phase data that can be produced by MRI scans and an example of a susceptibility map which can be constructed from the data (see figure 3).

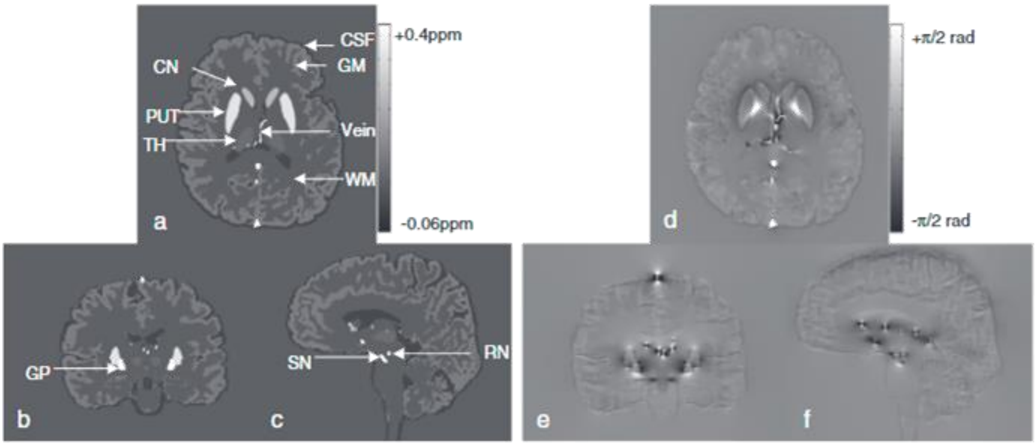

Figure 3. *Phase data of a simulated brain scan (right) and a corresponding susceptibility map (left). Acronyms on diagram: CSF = cerebral spinal fluid, SN = substantia nigra, WM = white matter, GM = grey matter, PUT = putamen, CN = caudate nucleus, RN = red nucleus, TH = thalamus, GP = globus pallidus (17).*

Practical QSM involves several image processing steps after the scan data has been acquired. Data from the set of receiver coils is combined and phase unwrapping steps are undertaken (17, 19). Local field variations are isolated through background-field removal. Background fields are defined as magnetic fields generated by sources outside of the area of interest being imaged. These fields are caused by variations in susceptibility and macroscopic currents in surrounding structures and are normally much larger than the field variations related to field sources in the region of interest (19). Without the removal of the background field, the areas where the region of interest meets the outside regions will be particularly difficult to deal with.
The phase offsets after these processes have been carried out are then deconvolved to produce information about the susceptibilities of the tissues in the region of interest (20).

1.2.4. MSDI

Acosta-Cabronero *et al*. have designed a bandpass filtering process, referred to as MSDI (multi-scale dipole inversion) which uses Laplace's equations to model and reduce noise in QSM mapping and is used in mapping software called "qsm-box", which is used later on in this thesis (20, 21).
The sum of susceptibility estimates from many Laplacian levels, *l*, can be used to calculate a phase distribution:

$$\phi'_l = (\delta - S_l) * \phi_l, \quad [36]$$

where ϕ'_l is the phase after high pass filtering, δ is the Dirac delta function and * is a 3D convolution operator. S_l is the spherical mean value (SMV)(19). This is a mathematical theorem which is often used in background field correction programs when considering field variation that can be described using a series of spherical harmonics inside of a spherical region. The theory is that the harmonic function calculated over a sphere is equivalent to the harmonic function at the centre of the sphere. The SMV is used in this situation in order to efficiently evaluate the internal field over space.

The phase distribution at scale *l*, can be described as the initial phase and the sum of susceptibility of the scales:

$$\phi_l = \phi - \mathrm{F}^H D \mathrm{F} X_{l-1}\,, \quad [37]$$

where F^H is the inverse Fourier transform and *D* is the dipole kernel in the frequency domain. The above equations (36 and 37) can be used without the phase distribution being unwrapped, however it is preferable to have performed a degree of background field removal before undertaking this process.

1.2.5. Static Dephasing Regime

The static dephasing regime is a regime in which the dephasing of MR signals due to any spatial inhomogeneity in the magnetic field occurs faster than the averaging of phases due to diffusion. This usually results in a larger accumulation of the phase and faster decay in the MR signal (1). This scenario is referred to as “static” as it occurs when motion of the atoms or molecules carrying nuclear spins is negligible. Large susceptibility variations, magnetic fields and length scales lead to the static regime being favoured (22).

In order to investigate the effects of static dephasing, stationary spheres inside a given volume should first be considered. The volume fraction of an object is given by equation 38 and relates the volume of an object (*v*) to the volume of the space of the system in which it is located (*V*). This has an impact on the field generated by an object at that point in space as well as the magnetic susceptibility of the medium and the external magnetic field applied.

$$\varsigma = \frac{v}{V}. \quad [38]$$

The signal generated by a gradient echo sequence pulse normalised over a volume, *V*, is defined as:

$$S(t) = \frac{1}{V}\int_{V-v} d(\vec{r})\rho(\vec{r})\exp[-i\omega(\vec{r})t], \qquad [39]$$

where ρ characterises the strength of the signal coming from each location, as well as the spin density, this depends on the sensitivity of hardware, flip angle and relaxation time. The local frequency generated by one perturber is calculated by considering a reference vector, $\vec{r_n}$, which defines the position of the nth perturber.

$$\omega_n(\vec{r} - \vec{r_n}) = \gamma \cdot b_n(\vec{r} - \vec{r_n})\,, \quad [40]$$

where b_n is the field generated by the perturber, which for a sphere of radius a is:

$$\gamma b_n = \delta\omega \frac{a^3}{r^3}(3cos^2\theta - 1). \quad [41]$$

where

$$\delta\omega_s = \frac{\gamma B_0 \chi}{3}. \quad [42]$$

Over a long time-scale ($\delta\omega_s \cdot t \geq 1.5$), the signal decays monoexponentially, and assuming that ρ is position independent:

$$\bar{S}(t) = \rho(1 - VF) \cdot \exp[-i\Delta\omega_s t] \cdot \exp[-R2'_s \cdot |t - t_s|]. \quad [43]$$

The "s" subscript is used as spherical particles are being considered, and VF is the volume fraction. The resulting relaxation time and frequency offset is given by equations 44 and 45 (1).

$$R_2{'}_s = \frac{2\pi}{9\sqrt{3}}(\gamma\chi B_0 VF), \quad [44]$$

$$\Delta\omega_s = -0.053(\gamma\chi B_0 VF). \quad [45]$$

The relaxation rate and average frequency offset are linked to the volume fraction of the spheres. As VF increases, R_2' and $\Delta\omega_s$ both increase.

1.2.6. Diffusion Effects on MRI

Brain tissue contains a large number of protons as a result of its internal water content (23). These water molecules diffuse randomly through the structure and interact with cells and as a result, information about the physiology and function of the brain can be evaluated (24). Diffusion in a body of water can be described by Brownian motion and the distribution of water molecules from the initial starting point can be shown to be a Gaussian distribution. When diffusion occurs in the body the displacement of the molecules is hindered by the presence of cell membranes and fibres often resulting in a Gaussian with a smaller standard deviation compared to unhindered diffusion.

When water molecules diffuse through the magnetic field gradients applied during the imaging process over a given time (the diffusion time, τ_D) a phase shift in the MRI signal is generated (25). Over a single image voxel this changes the phase shift distribution and affects the coherence of the MR signal, so producing an attenuation in the measured signal (25). The attenuation of the signal can be calculated using the following equation:

$$\frac{S}{S_0} = \exp(-b\ ADC), \quad [46]$$

where b is the diffusion sensitization which is a parameter that describes the amplitude and duration of the gradient pulses which are used to encode the molecular diffusion and ADC is the apparent diffusion coefficient. The ADC is a concept which was developed for diffusion MRI as diffusion occurring inside the brain and body does not follow a standard Gaussian distribution and therefore cannot be described as simple Brownian motion.

Diffusion of water molecules in local spatially varying magnetic fields can also reduce the phase difference between magnetic moments of nuclei. This scenario is referred to as the motional narrowing effect and occurs when $\delta\omega \cdot \tau_D \ll 1$ (where $\delta\omega$ characterises the range of frequency offsets due to the field perturbation) and τ_D is comparable to the time taken for the molecule to diffuse over a distance equal to the size of the particle which is generating the magnetic field (25).

Flow of water, and by extension the flow of blood, can change signal intensity and as a result there are several imaging techniques that have been developed to take advantage of this. One technique is arterial spin labelling (ASL) which is a process used to measure perfusion effects in the brain when investigating cerebral blood flow. An inverted RF pulse is applied to blood in the arteries, polarising the water molecules. A T_1 image is taken after a short delay to allow for the molecules to flow into the imaging plane and diffuse into the brain tissue. Another image is taken when there is no treated blood present and this is subtracted from the previous image to evaluate the difference in signal. The difference in intensity is proportional to the amount of blood delivered to the tissues over that period of time (26).

1.2.7. Iron and the Brain

Throughout the body, iron is used as a means of transporting oxygen in the form of haemoglobin. In the brain, iron has other uses, such as manufacturing neurotransmitters, creating myelinated sheathes, and maintaining enzyme function (27, 28). Once ingested, iron is absorbed in the digestive system aided by ferroxidase hephaestin (29) in ferrous ($Fe2+$) form. Once the iron has entered the circulatory system it binds to transferrin as ferric iron ($Fe3+$) before being released to cells to use in metabolism.

Hepatocyte cells are responsible for storing and detecting the total iron levels in the body and regulating the absorption of iron by releasing the hormone hepcidin. Iron returning to the circulatory system is dictated by macrophages controlling the expression of ferroportin, a substance used to export iron back into circulation. When hepcidin production has increased, it binds to the cell membranes of macrophages which causes ferroportin to degrade. The reduction in the expression of ferroportin slows the rate of iron absorption in the intestine and the amount of iron being returned from the circulation system, and therefore reduces the levels of iron in body serum (28). Iron is also present in the brain and enters through the blood brain barrier (BBB) with the aid of endothelial transferrin receptor (TfR) expression (29, 30).

Iron concentration is regulated in the brain, as an excess will form hydroxyl radicals, leading to oxidative stress, neuron death (31), and damage to DNA (32). Ferritin is a protein complex used to store iron and is found both intracellularly and extracellularly (33). A spherical protein shell (which contains no iron) called apoferritin forms a container which holds ferric iron in the form of ferrihydrite materials (33).

Alzheimer's disease, one of the most common neurodegenerative diseases, effects over 10% of the UK's population (34) and is a disease which causes memory functions deteriorate (35, 36). There is a build-up of iron in the brain due to altered iron homeostasis and the breakdown of myelin. This excess of iron is often associated with masses of decaying neurons called senile plaques, which are particularly found in the hippocampus. A study carried out by Smith *et al*. (37) used a histochemical analysis method on post mortem brains to evaluate the difference in iron levels in the hippocampus in subjects with AD and in healthy controls. They found that the iron associated with lesions in the AD brain had high redox activity which can lead to oxidative damage to cells.

Patients with AD experience atrophy in various sections of the brain such as in the hippocampus as the disease progresses (38). Structural and QSM MRI scans can be used to track the changes in the hippocampus in vivo. Antharam *et al*. (39) showed that there was an increased R_2* in brains which suffered from AD compared to healthy controls due to the increased levels of iron present. The study also found that the properties of water diffusion in the brain changed due to degradation of the tissues leading to a reduced relaxation time. Diffusion tensor imaging has also shown that both white and grey matter is affected by AD which results in changes in the thalamus and hippocampus leading to cognitive functions becoming impaired (40).

Neuromelanin (NM) is a dark pigment, found in high concentrations in the substantia nigra (SN) and locus coeruleus (LC). Degenerative and x-ray diffraction studies (8, 40) have shown that NM has a three-dimensional lattice arrangement consisting of cyclic molecules and indolebenzothiazine rings, with dopamine and cysteine making up most of the structure. NM has neuroprotective qualities as it can protect against neurotoxins, such as MPTP, and other organic compounds (40). NM binds to several different elements such as copper and zinc, but it has the biggest affinity with iron. Ferric iron found in the SN is chelated by NM, binding iron ions and therefore protects neurons from oxidative stress (41, 42). It has been seen (40) that this NM maintains a residual chelating capability by only being 50% saturated with Fe(3+).

Parkinson's disease (PD) is a neurodegenerative disorder in which the neurons in the basal forebrain die. The disease is normally diagnosed when motor functions are affected and when at least 30% of the neurons in the SN have died (8, 42). When neurons die, microglia cells break down NM, releasing hydrogen peroxide, which oxidises and degrades more NM pigment, trigging further neurodegeneration (42). The levels of NM and ferritin in the brain increases in the first few years of aging in healthy individuals, however patients with Alzheimer's disease (AD) and PD have shown levels of 50-60% of the age-matched controls (42). Iron concentration in the SN can increase by up to 30-35% in patients with PD and other similar disorders (40).

The LC and SN can be imaged using magnetic resonance imaging. Neuromelanin and ferritin are paramagnetic due to their iron content and NM in particular affects magnetisation transfer between bound and free pools (43). Figure 4 shows an example of a T_1-weighted image with associated magnetisation transfer contrast of the SN in the brains of a healthy control (left and middle) and a patient with PD (right). This study carried out by S. Prasad *et al*. showed signal intensity of the SN in the PD patient was reduced due to neuronal death (44).

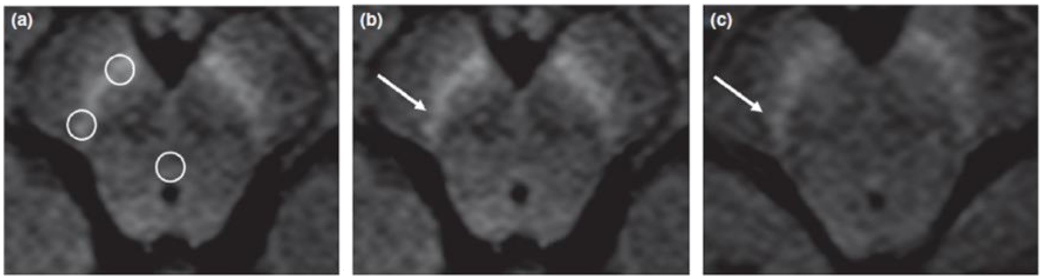

Figure 4. *Arrows point towards the SNc. The three circles show the different regions of interest used to assess the changes in signal intensity (44).*

A study carried out by Sasaki *et al*. investigated neurons in the SNc and LC which contain neuromelanin (45). A 3T MRI scanner was used to image 17 patients with Parkinson's disease and the signal intensity of the LC and SNc was compared with healthy, aged matched controls. The images obtained were fast spin echo T_1 weighted images, and the signal intensities of the regions of interest were measured in a blinded manner. It was found that the signal intensity of the LC and SNc was reduced in the patients with PD by a statistically significant amount. The authors suggested that their study could be improved upon by improving the image quality as the LC is very small and therefore the neurons in the LC are difficult to localise accurately. Image resolution would be improved by using a scanner with a higher field strength.

2. Modelling of Dipole Fields

Contents

This chapter describes the process of modelling the effect on the NMR signal evolution of a single spherical field perturber in the absence of diffusion. This work is then extended to include simulations that take into account the effect of multiple perturbers and also to consider the effect of diffusion of spin-bearing molecules in the magnetic field distribution. Analyses of the signal magnitude and phase are carried out.

2.1. Modelling a Stationary Dipole Field

The aim of this initial work is to investigate how well computer simulations can model the effect of a single spherical perturber on the NMR signal evolution in the static dephasing regime. The data produced was compared to the work carried out by Yablonskiy and Haacke (21) in order to evaluate how successfully the simulation can model the static dephasing regime.

2.1.1. Method

Computer simulations were carried out using algorithms written using MATLAB R2018a (Mathworks, MA, USA). The magnetic field due to a spherical perturber was modelled by placing a sphere of radius r= 1µm, which was equivalent to 10 voxels, with a volume magnetic susceptibility of $\chi = 1\times10^{-6}$ inside a spherical space. This size was chosen so that the size of the simulated perturber would be of the same order of magnitude as other common perturbers found in the body, such as red blood cells and ferrite particles (1). A homogeneous magnetic field (B_0) which had a field strength of 7T was added. This was chosen, as the field strength to be used in future studies carried out at the University of Nottingham, SPMIC will be 7T. The field within the sphere was constant. A spatially varying field perturbation created outside the sphere was then calculated using equation 47, which is the unit dipole field described in equation 33 multiplied by the dipole moment due to the magnetisation in the sphere

$$B_z = \frac{\chi V B_0}{4\pi}\left(\frac{{3z^2}/{r^2} - 1}{r^3}\right), \quad [47]$$

where V is the volume of the sphere. Equation 47 calculated a 3D field. In order to view a 2D slice of the field a plane that cut through the middle of the space was isolated. The resulting image showed the field as a very tiny point within the space. In order to see a detailed shape of the dipole, a mask was created to force the image displayed to zoom in on the area of interest.

The mask was created by constructing a space where every voxel within the spherical coordinate array was equal to one.

Figure 5 shows the value of B_z over space, where the x and y axes show voxel number and the colour bar shows the value of Bz. The centre point of the space was (101,101).

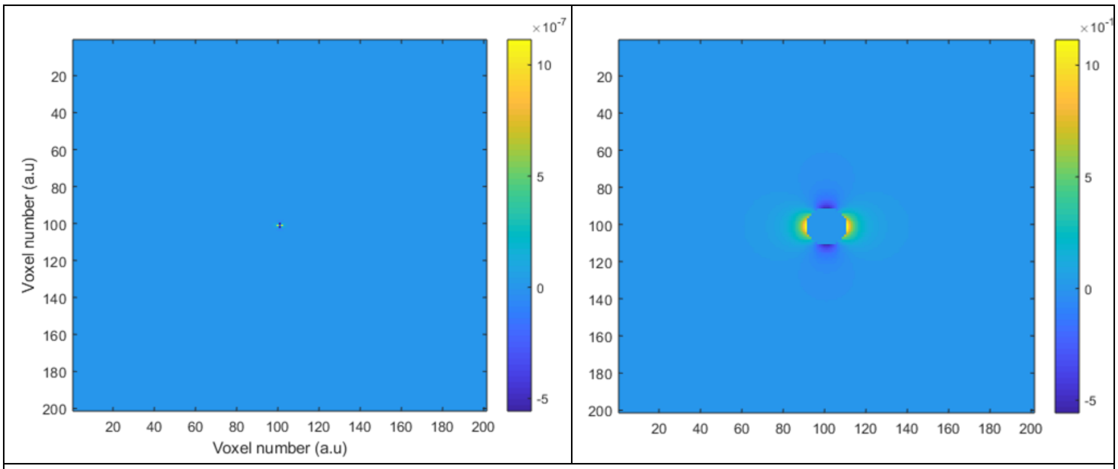

Figure 5. *Magnitude of B_z, cutting through the centre of the X plane. Left shows B_z, right shows "zoomed in" B_z after mask application. The colour bar represents the magnitude of the field.*

The phase offset due to the field, B_z after the signal has evolved for time τ was calculated using equation 48 and was then shown as an image (see figure 6). The images were taken in the same plane as the images above.

$$\phi = \gamma \tau B_z. \qquad [48]$$

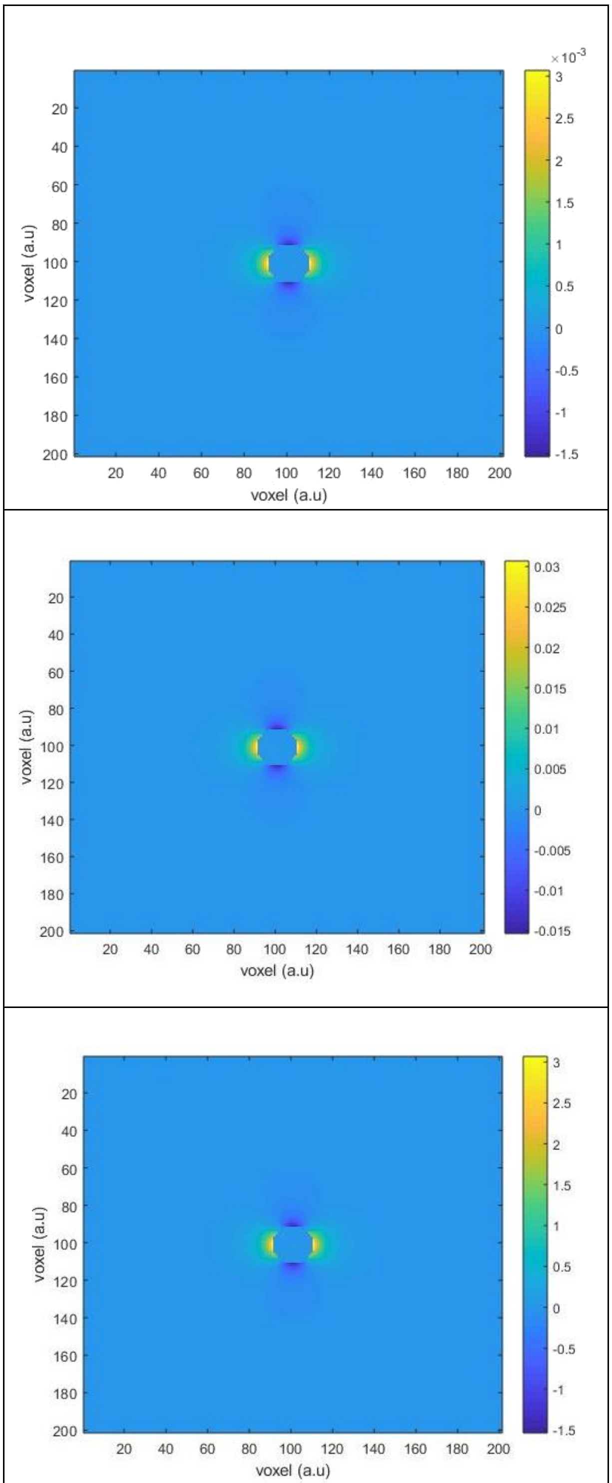

Figure 6. *Phase due to B_z at various τ values. Magnitude of phase is shown by the colour bar in radians. Viewed top to bottom, images shown are τ= 1 ms, τ=10 ms and τ=1 s respectively.*

The signal generated by the dipole, starting with τ=0 s, was calculated using the phase previously calculated and equation 49.

$$S = e^{i\phi}. \qquad [49]$$

This calculation produced an array of numbers representing the signal across the three-dimensional space. A complex sum of the signal across all of the voxels was taken and stored in an array. The time was increased and the phase and signal were recalculated and stored in the array. This process was repeated until one thousand iterations had been performed. The data could then be plotted to show the signal evolving over time.

It was theorised that the signal is directly related to the volume fraction of the space occupied by the spherical perturber (1). In order to test this, the size of the space in which the sphere was sited was varied and the simulation was repeated.

An array of randomly positioned spherical perturbers was then added into the simulation in order to look at how they changed the signal and phase evolution of the system and this was then modified in Chapter 2.3 to look at diffusion in magnetic fields. A sub code (see appendix 1) was used to calculate the field disturbance due to an array of spherical perturbers present in the space and this was used to create a field map and hence gather signal and phase data.

2.1.2. Results and Discussion

The phase and magnitude images (see figures 5 and 6) successfully showed a dipole field. It can be seen from the yellow and dark blue areas on the image that both positive and negative fields are being produced.

Initially one susceptibility value was tested in order to establish whether the model was producing sensible results. Figure 7 shows the result of using $\chi = 1 \times 10^{-6}$. An exponential decay of the signal magnitude was seen to occur over time. Two other susceptibilities were then evaluated ($\chi=1 \times 10^{-5}$ and $\chi=1 \times 10^{-6}$) and the results were plotted graphically (see figure 7).

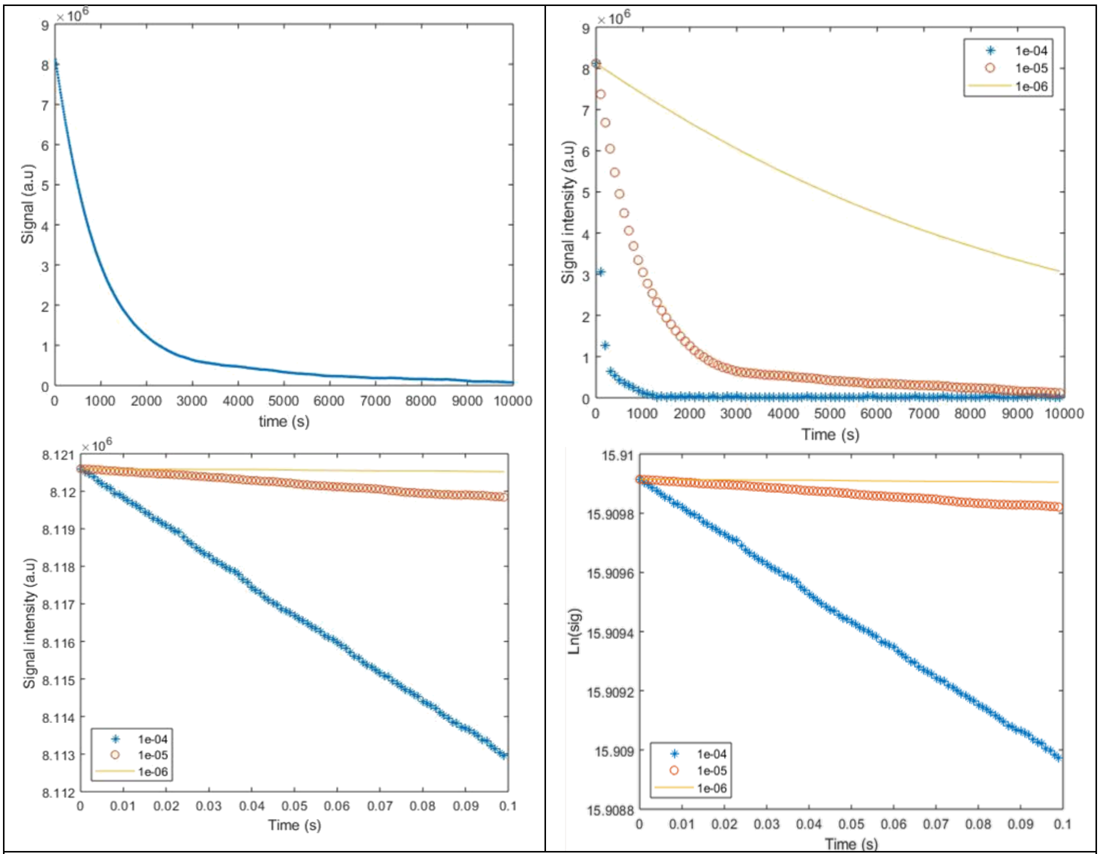

Figure 7. *Signal produced by a single dipole over time (top left). The right hand graph shows the signal intensity using three different susceptibilities (χ=1x10^{-4}, χ=1x10^{-5}, χ=1x10^{-6}), and the bottom two graphs show a "zoomed in" section and the natural logarithm of the graphs above. VF=1x10^{-6}.*

It was seen that the signal decayed faster with larger magnetic susceptibilities. This was expected as the magnetic susceptibility describes how easily a material is magnetised when exposed to a magnetic field. External magnetic fields will cause more induced magnetisation in materials with large magnetic susceptibilities, and so the external field perturbation is larger. Dephasing consequently occurs more rapidly and the signal decays faster as the susceptibility is increased.

The average frequency of the signal was calculated from the gradient with respect to time of the signal phase. The frequencies of the signal for two of the susceptibilities considered can be seen in figure 8. Using the large susceptibility in the simulation caused the variables used to vary very quickly between neighbouring voxels, resulting in an unreliable and unrealistic signal and frequency.

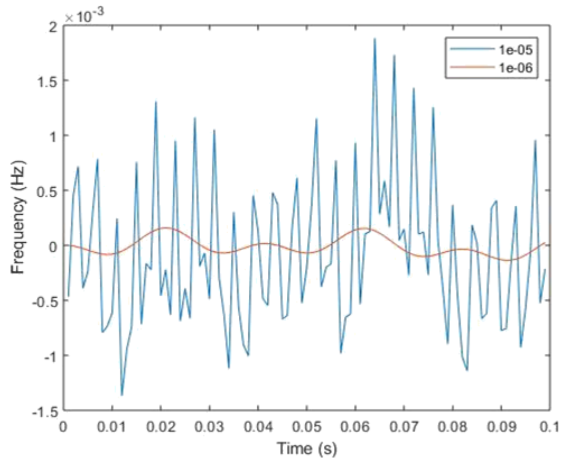

Figure 8. *Frequency data from a signal dipole using two different magnetic susceptibilities (χ=1x10^{-5} and χ=1x10^{-6}). VF=1x10^{-6}.*

After the volume fraction had been reduced from 8x10^{-6} to 1x10^{-6} the simulation was run again and the graphs in figure 9 were produced.

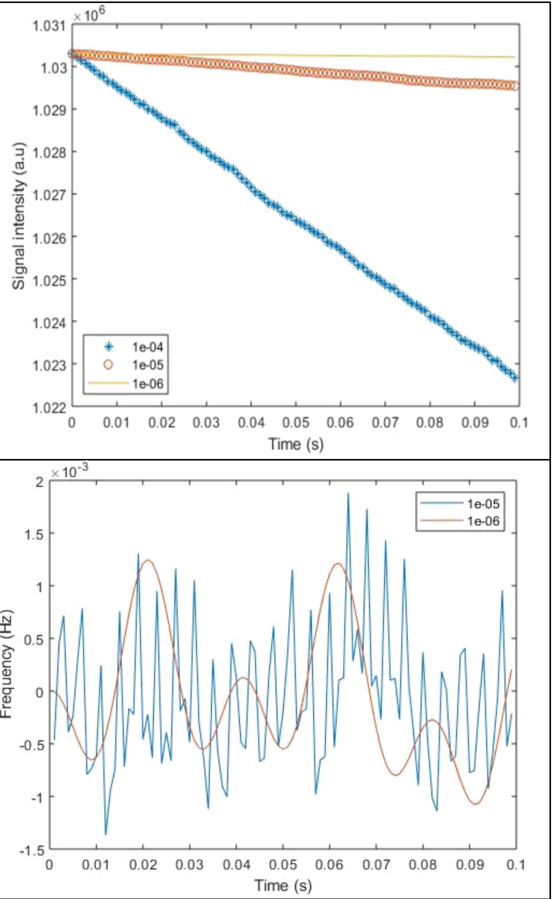

Figure 9. *Data produced after the volume fraction was reduced by a factor of 8. Signal data (top) and frequency data (bottom). χ=1x10^{-5} and χ=1x10^{-6}. VF=1x10^{-6}.*

Figure 10 shows a direct comparison of frequency data for two different volume fractions (VF= $8x10^{-6}$ and VF=$1x10^{-6}$).

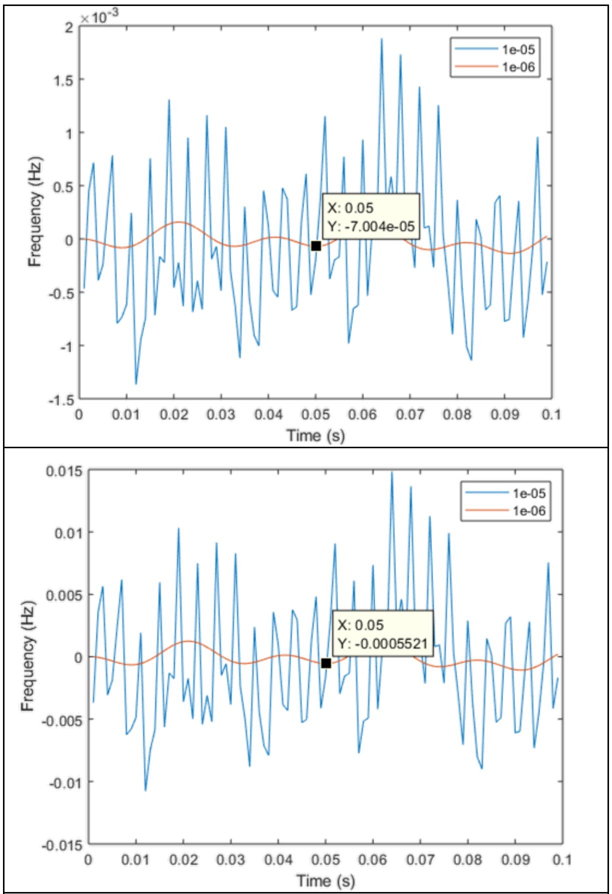

Figure 10. *Graphs showing frequency and phase data from the simulation. The graph on the top shows VF=$1x10^{-6}$ and the graph on the bottom shows VF=$8x10^{-6}$.*

The data cursor tool was used to select the data at evolution times of around 0.05s. The data before this point was not considered as the signal data was not linear. This is due to the relationship which is described by Yablonskiy *et al*. (1) which states that for short time scales the signal decay follows a quadratic exponential relationship. In order to analyse a monoexponential signal decay, timescales relating to $\delta\omega \cdot t \geq 1.5$ should be considered.

The frequency and signal data could then be compared. The frequency data from VF=$8x10^{-6}$ was divided by the data from VF=$1x10^{-6}$ to obtain a number representing the scaling factor for each data point. This number was then averaged to get an average scaling factor which described how much the frequency increased when the volume fraction was changed. An error associated with this was calculated using standard error. It was found that when the volume fraction was multiplied by a factor of 8, the frequency increased by a factor of 7.88434(±0.00024) and the exponential rate of decay of the magnitude signal increased by a factor of 7.88(±0.05). This was true for both susceptibilities.

The simulation was repeated and R_2* was calculated from the signal data at several different volume fractions. The results can be seen in figure 11.

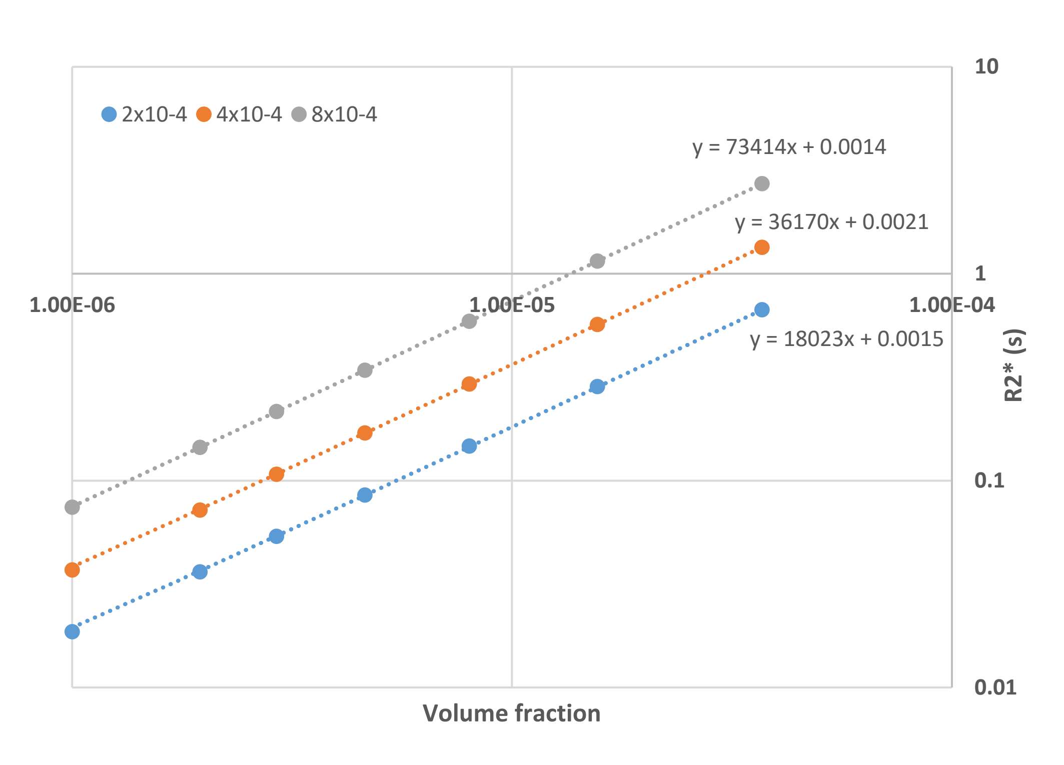

Figure 11. *A graph showing how volume fraction effects R_2* for three different susceptibilities. Susceptibilities shown are $2x10^{-4}$ (blue), $4x10^{-4}$(orange) and $8x10^{-4}$ (grey).*

It was seen that R2* was proportional to volume fraction for every susceptibility value used.

To make a direct comparison to the Yablonskiy paper (1) the magnitude of the gradient of the phase evolution with time was calculated and averaged. This process was repeated for susceptibility values of $2.0x10^{-4}$, $4.0x10^{-4}$ and $8.0x10^{-4}$ and $\gamma=267.5x10^6$ $rads\cdot s\cdot T^{-1}$. The mean of the gradient of the log of the signal magnitude was also found for each susceptibility and this was used to find R_2'. These results were plotted on a graph against the value of $\gamma\chi B_0VF$ (see figure 12). The slope of these lines can be used to verify whether the simulation agrees with literature values (1). By revisiting equations 44 and 45 from section 1.2.4:

$$R_2{'}_s = \frac{2\pi}{9\sqrt{3}}(\gamma\chi B_0 VF), \qquad [44]$$

$$\Delta\omega_s = -0.053(\gamma\chi B_0 VF). \qquad [45]$$

It was seen that plotting the newly calculated phase data and signal data against $\gamma\chi B_0 VF$ resulted in a graph with a gradient which can be directly compared to literature.

The accuracy of the results produced by the simulations carried out in this thesis was estimated by taking the ratio with the values calculated using the theory described in the Yablonskiy paper (1).

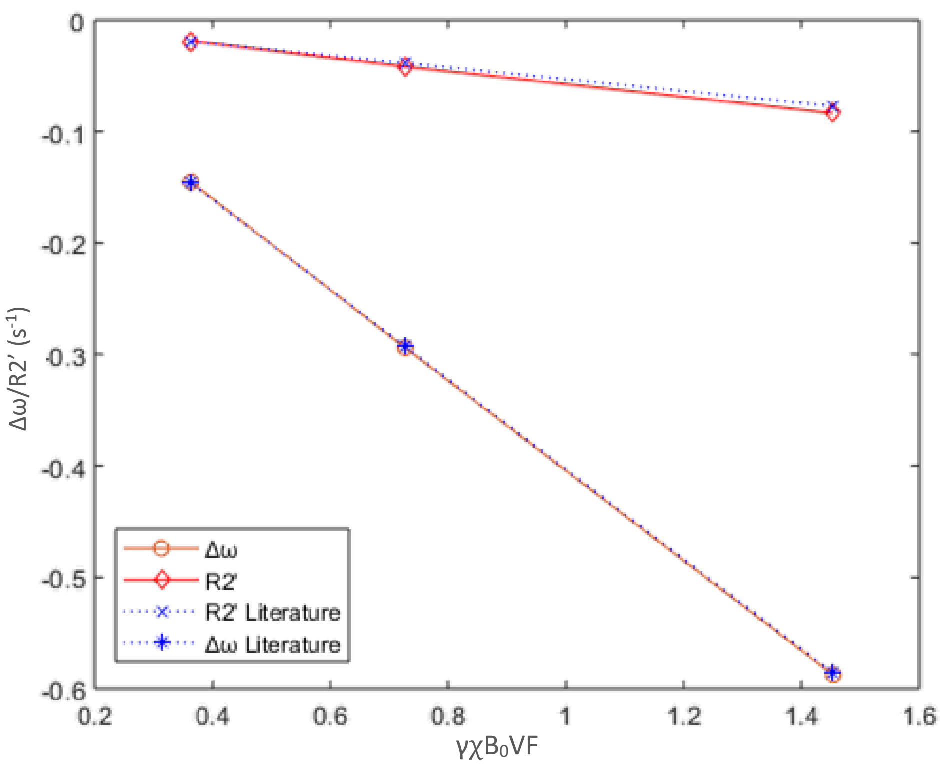

Figure 12. *A graph showing $\Delta\omega_s$ (orange circles) and $R2'_s$(red diamonds) for three different susceptibilities. The gradient of the two trendlines was found and compared with literature values (blue crosses and stars).*

Table 1 shows the calculated coefficients which are compared to the coefficients in equations 44 and 45 from the literature. The accuracy of each value is also shown.

Gradient of ln(signal) = R_2' (s^{-1})	-0.4054
Ratio to theoretical value of R_2'	1.006
Gradient of phase line = $\Delta\omega_s$ (s^{-1})	-0.0590
Ratio to theoretical value of $\Delta\omega_s$	1.07

Table 1. *Results of comparing data obtained from simulation to the expected values taken from Yablonskiy's work (1). Susceptibility values were 2.0×10^{-4}, 4.0×10^{-4} and 8.0×10^{-4} and $\gamma = 267.5 \times 10^{6}$ rads·s·T^{-1}.*

The slope of the phase data was accurate to within 6% and the calculated R2’ value was within 0.6% of the literature value.

The simulation effectively modelled the static dephasing regime with an acceptable bound of error. The errors could be reduced by investigating a wider range of susceptibility values in order to get more data points for the graph in figure 12. More data points would provide more confidence in the best fit line and therefore produce a gradient which was more reliable.

The algorithm successfully modelled a single sphere. The results of this experiment agreed with the Yablonskiy (1) paper within an acceptable margin of error. This is important as the results confirm that the model created can accurately model a singular sphere and hence can then be developed to model a system with a random array of spheres. Using a random array of spheres would be a more realistic when modelling real tissues and processes occurring inside living tissues.

Processes such as QSM rely on the assumption that each of the voxels being examined have uniform properties. In order to generate a QSM map the overall field at each voxel is measured and inverted. Yablonskiy *et al*. theorised that there is an inhomogeneity inside each voxel (1). If there is any inhomogeneity in the field which is not accounted for, the field map will not provide an accurate representation of the material. Voxels containing magnetic perturbers are no longer homogeneous as the field experienced by a particle would become weaker with distance from the perturber. This would result in a different phase evolution over time compared to if the voxel was homogeneous. If no perturbers were present the uniform field assumption would be correct as a uniform field would be seen due to positive and negative fields balancing each other out over large areas.

2.2. Modelling the effect of diffusion

The model used to evaluate the effect of a single spherical perturber (see section 2.1) was modified to create a simulation of an array of particles randomly diffusing in the magnetic field distribution produced by a random distribution of spheres. This was achieved by creating a random walk algorithm to allow the particles in the simulation to mimic Brownian motion. Signal magnitude and phase evolution were evaluated and relaxation times and average frequency offsets were calculated for scenarios with different magnetic susceptibilities.

2.2.1. Method

The first step in modelling the effect of diffusion was to create an algorithm that produced a “random walk”. This initially considered a hundred particles, which moved randomly in one dimension with each iteration of a for loop. In this simulation $1x10^5$ particles were then considered. One iteration of this loop was used as an arbitrary time step. The particles were moving randomly and this was seen by taking a measurement of the standard deviation of the displacement histogram at various times after the start of the random walk. This process was repeated using and 100 time steps. A histogram showing the displacement of the particles after 100 steps can be seen in figure 13.

The standard deviation was calculated and was displayed as a line on the histogram showing a Gaussian distribution.

The random walk algorithm was then modified to include a random walk in three dimensions and was integrated into the sphere simulation model from section 2.1 to create a simulation of randomly moving particles in a spatially varying magnetic field to generate a complex signal whose magnitude and phase was subjected to further analysis to evaluate decay rate and average frequency.

Initially 1000 particles were randomly positioned within the simulation as this allowed the algorithm to run quickly. However, the number was then later increased to 10,000 particles after it was shown that the program could run without errors and showed sensible results. The field perturbation produced by the random arrangement of spheres was calculated.

The distance travelled by a particle after each step was changed by altering a parameter called “n_D”. This describes the number of voxels to be jumped at each step of the random walk. By increasing this number, the particles moved a greater distance simulating faster diffusion. If a jump took a particle inside a perturber the jump was not allowed and the particle did not move at that time-step.

Complex signals were generated by averaging over several randomly generated arrangements of spheres. With each repeat a block of 256 voxels was considered and this data was then summed together to create data which represented a much larger space, whilst keeping the processing power and memory capacity needed to run the model at a manageable level. Initially the number of repeats started at 1 but was later increased to 80. Increasing the number of repeats increased the amount of time it took to run the simulation significantly. When using 1 repeat and 1000 particles the model only took about a minute to run but after increasing to 80 repeats with 10,000 particles it took 40 minutes for a complete run.

The model also saved the data to an Excel (Microsoft Excel 2016) spreadsheet so that analysis could be carried out at a later time.

The random walk algorithm and the final diffusion model can be found in Appendix 1.

2.2.2. Results and Analysis

In the simulations of simple diffusion in one dimension, particles started off at the same central position and should have slowly moved outwards and away from the centre. This was tested by considering the root mean squared displacement (rms) of the particles over time. The standard deviation of a Gaussian curve can be related to the rms using equation 50.

$$< x^2 > = \sigma. \quad [50]$$

Standard deviation is linked to the amount of time elapsed during diffusion using equation 51.

$$\sigma = \sqrt{2Dt}, \quad [51]$$

where D is the diffusion coefficient (46).

The diffusion coefficient can also be defined by considering the size of each voxel, Δr and the timestep used. The size of the jump made by a particle undergoing diffusion is defined as $n_D \Delta r$ in each dimension. Using a timestep of Δt , the diffusion coefficient, with units of m^2s^{-1}, can be calculated using equation 52 for diffusion in three dimensions:

$$D = {n_D}^2 \frac{\Delta r^2}{6\Delta t} \quad [52]$$

The variation of n_D can be viewed in terms of a change in the perturber size with a fixed diffusion coefficient. If a diffusion coefficient of $1\text{x}10^{-9}$ m^2s^{-1} and a time-step of $2\text{x}10^{-4}$ s is used the voxel size in three dimensions is effectively defined by equations 53 and 54.

$$\Delta r = \frac{\sqrt{6D\Delta t}}{n_D}, \quad [53]$$

$$\Delta r = \frac{1.905\text{x}10^{-6}}{n_D}. \quad [54]$$

For the algorithm to successfully model diffusion, the standard deviation of the distribution of particles should increase with the square root of time. This was seen as the standard deviation increased from σ=1.16 (±0.12) after one time-step to σ=3.33 (±0.33) after 10 time steps. The errors were calculated using standard error. The distributions of 100 particles and 10,000 particles can be seen in figure 13.

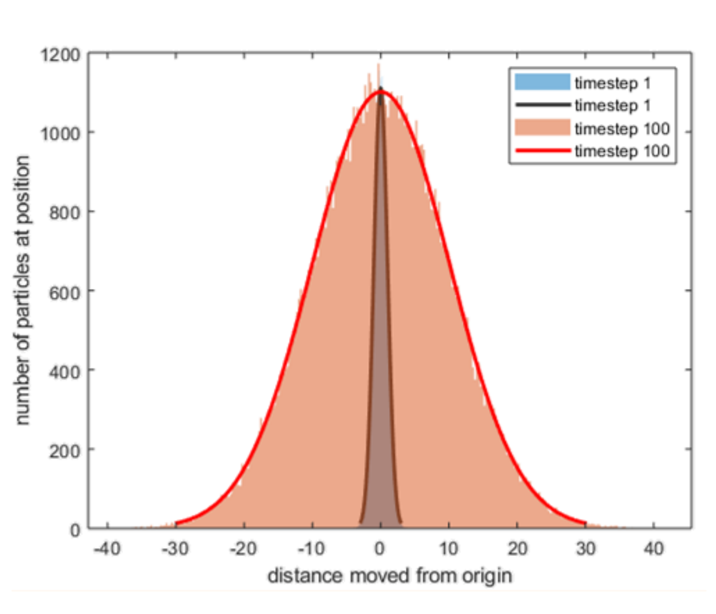

Figure 13. *Distribution of 1x10^5 particles after 100 time steps. Timestep 1 had σ=0.9993 (±0.0064) and timestep 100 had σ=10.05(±0.47). Histogram plotted with 316 bins.*

The standard deviation should scale with the number of time-steps (see equation 52) in order to be a successful model for diffusion. The standard deviation data for 10 timesteps was recorded and plotted on a graph and can be seen in figure 14.

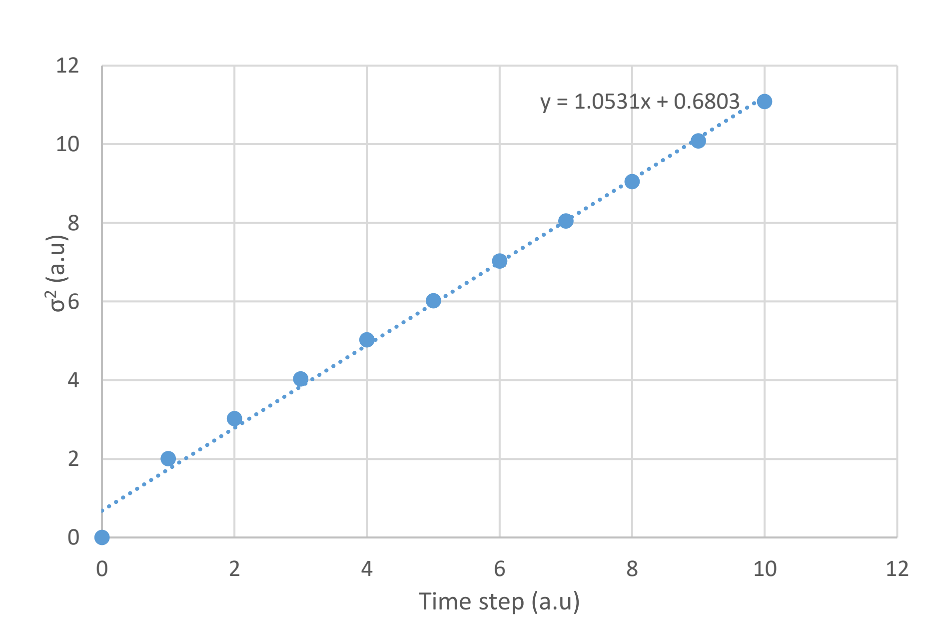

Figure 14. *A graph displaying how σ^2 varied with time. 1x10^5 particles were used. Standard error is shown on the graph, but this was very small due to the large number of particles used.*

The relationship between σ^2 and time which is shown in figure 15 was seen to be linear which agrees with equation 51. The gradient of the line and its associated error was found using the 'linest' function and had a value of 1.053 (±0.026). When comparing this to the theory, it is assumed that a diffusion coefficient of D=0.5 was used.

Data was generated using equation 51 using two different diffusion coefficients and was plotted graphically (see figure 15). The data from the model produced results which agreed within the bounds of error with the calculated data when a diffusion coefficient of $D=0.5m^2s^{-1}$ was used.

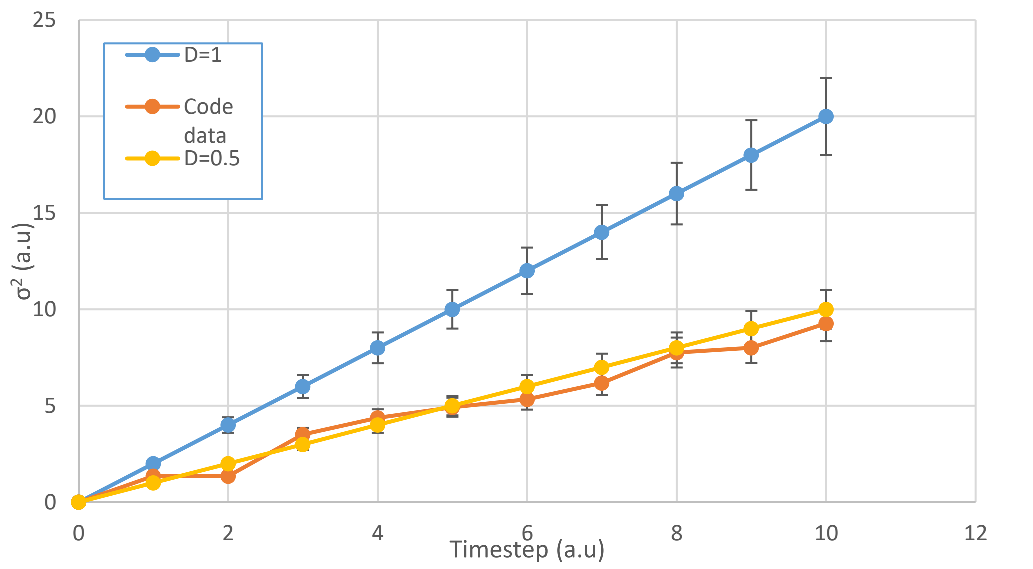

Figure 15. *A graph showing standard deviation (sigma) after each timestep for the simulated and calculated data. Error bars show standard error.*

At timestep 2 the standard deviation did not fit the general shape of the quadratic curve. This data point was not considered anomalous as the upper error limit still agreed within the bounds of error with the expected sigma values. The standard deviation did not have a perfectly quadratic relationship, but this may be due to the random number generator used in the model. The randomness resulted in Gaussian curves which were skewed slightly in one direction. Small values of timestep did not fit the expected trend due to the fact that the jump size has discrete values and so at a timestep of 2 the only jumps that the particles can take are displacements are -2, -2, 0, 1 or 2. A larger number of time-steps should be considered to accurately model diffusion. After the random walk algorithm had been integrated into the diffusion simulation, the signal produced over time was evaluated and different n_D values were used. The resulting signals can be seen in figure 16. In all of these simulations the random walking particles were not allowed to jump inside a spherical perturber.

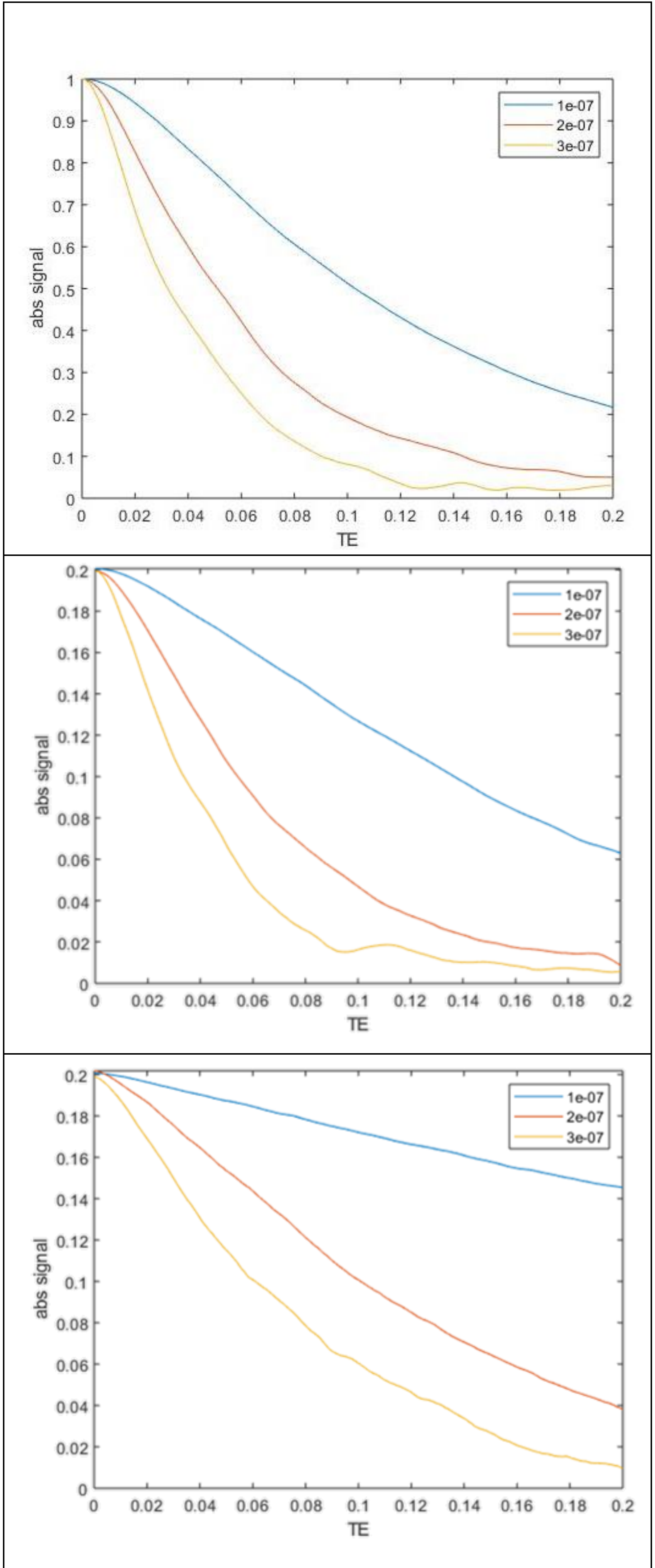

Figure 16. *Signal observed from diffusing particles over time. Graphs shown are for n_D=1 (top), n_D= 2 (middle) and n_D=5 (bottom). Susceptibilities investigated were; χ=1.0x10^{-7} (blue), 2.0x10^{-7} (orange) and 3.0x10^{-7} (yellow). VF=1.0x10^{-6}.*

By using equation 54, the particle sizes can be calculated for each n_D value. The simulations seen in figure 15 were χ=1.0x10^{-7}, 2.0x10^{-7} and 3.0x10^{-7} and so the corresponding particle sizes for each simulation are 1.9x10^{-6}, 9.5x10^{-7} and 3.8x10^{-7} respectively.

In order to evaluate how the diffusion process affected the signal evolution, the magnitude and phase data produced for each susceptibility was analysed and $\Delta\omega_s$ and $R_2{}'_s$ were calculated and plotted graphically using the same method as in section 2.1.2.

According to Yablonskiy *et al* the signal detected is related to the relaxation time and hence T_2* (1) (see equations 24 and 25). By plotting a graph of the log of the signal against time a linear graph is created and R_2* can be determined from the gradient. An example of one of these graphs can be seen in figure 16. This was made using the same three susceptibility values used in section 2.1 but with a diffusion step Tj=2.

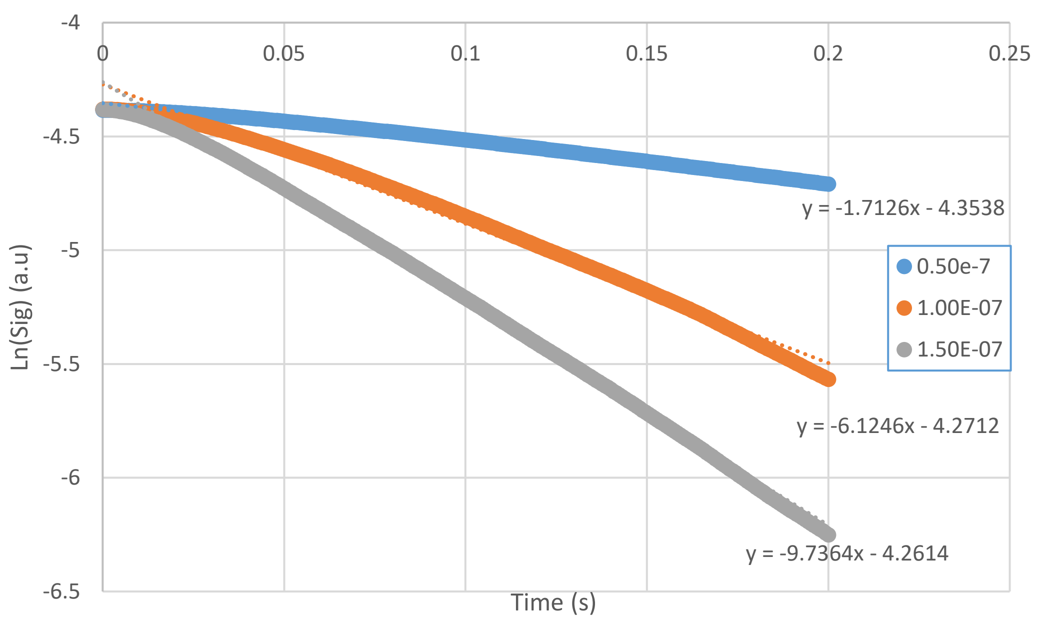

Figure 17. *Ln of the magnitude of the signal data when using a diffusion step of 2. The graph is not linear at the beginning but becomes linear after ~ 0.05s.*

In order to use the previous equations to calculate the relaxation times a linear section of the graph needs to be considered. According to Yablonskiy *et al* (1). for time scales which exceed $\delta\omega_s \cdot t \geq 1.5$ the signal experiences a monoexponential decay. Before this scale however a quadratic exponential decay is observed. After plotting all of the data on a graph it was estimated that the above graph became mostly linear after 0.05s and as a result the data after this time was then analysed and the rest was ignored. The new graph which was plotted can be seen in figure 18.

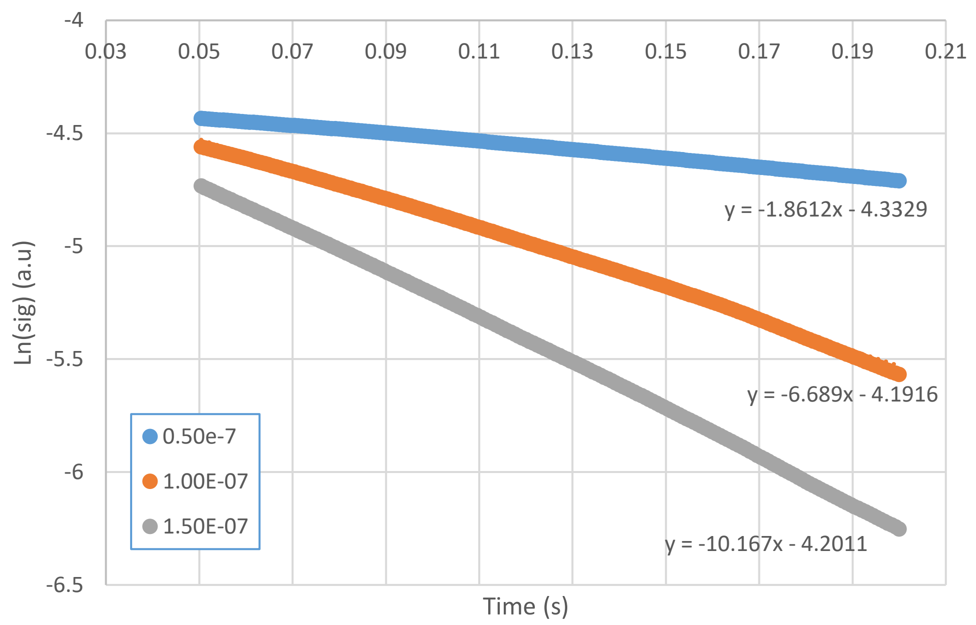

Figure 18. *The range of data considered whilst using n_D=2. The x-axis starts from t=0.05s as the data gathered before this was not linear.*

Linear regression was carried out using the "linest" function on Excel. This used the least squares method to plot a linear trend line on the data and then gives a value for the gradient along with its associated error. This process was repeated for four different diffusion steps and three susceptibilities. The resulting relaxation times can be seen below in figure 19. Error bars displaying the error calculated by linest have been plotted but they were too small to be seen on this graph.

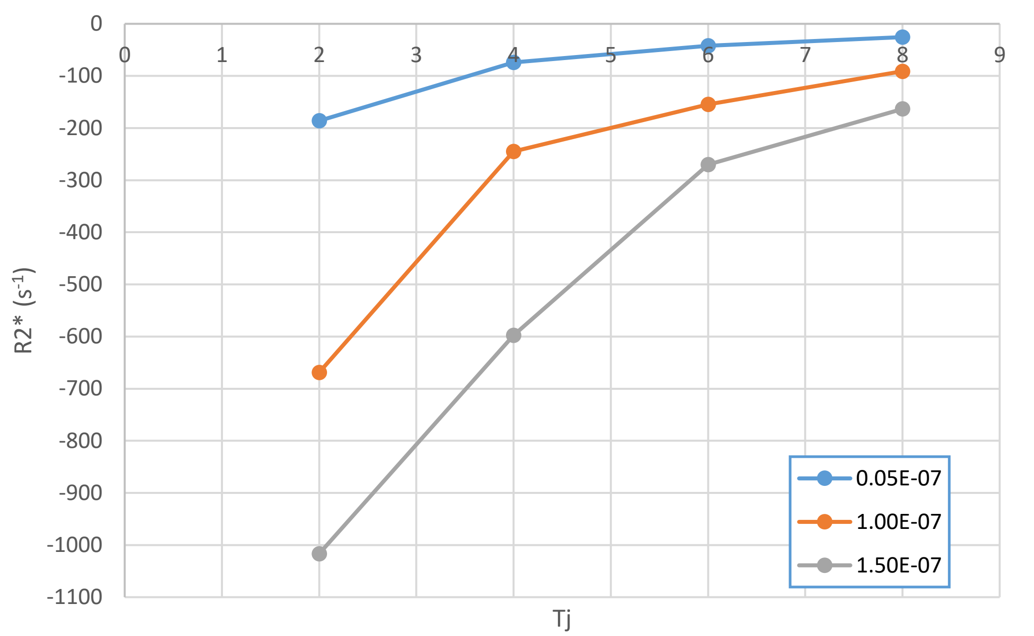

Figure 19. *A graph showing how R_2* is affected by diffusion for different magnetic susceptibilities. A table showing the numerical data used to make this graph can be found in appendix 2.*

Graphs displaying how the signal and frequency evolved over time with two different jump sizes can be seen in figures 20 and 21.

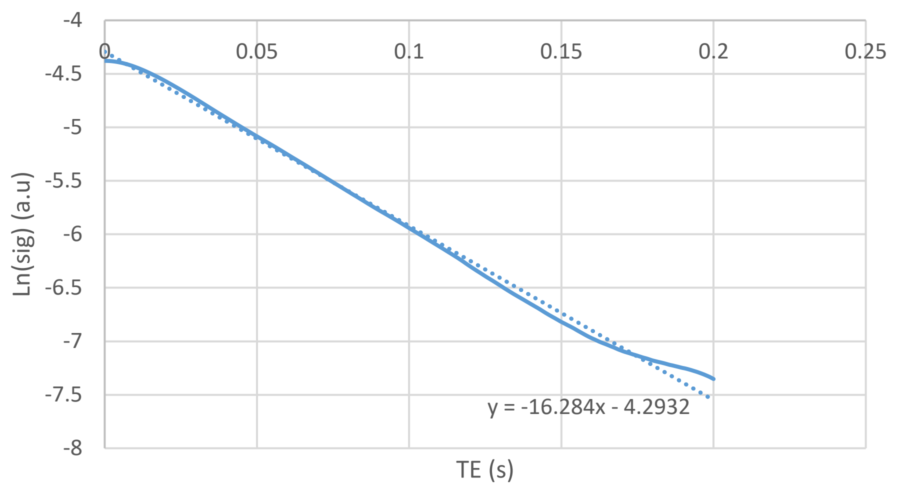

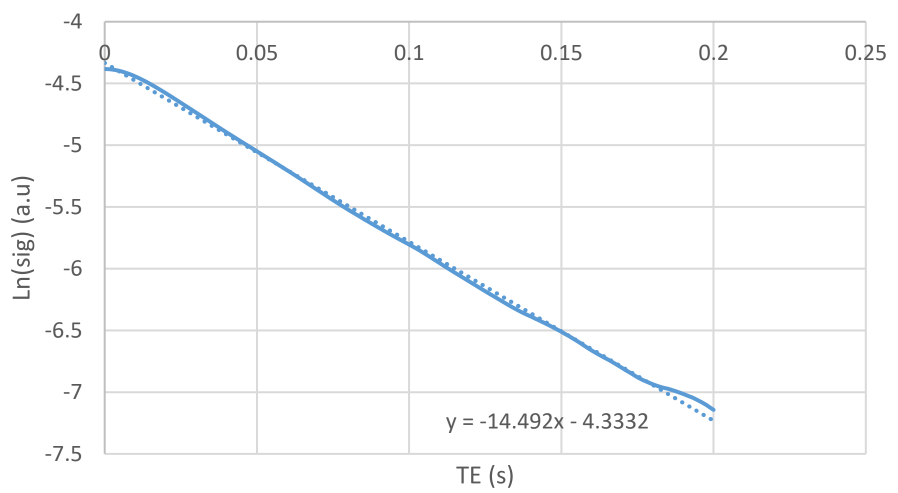

Figure 20. *Log of the signal magnitude over time for 10,000 particles diffusing inside a magnetic field. The top graph shows n_D=2 and the lower graph shows n_D=6. χ=2x10^{-7} for both simulations.*

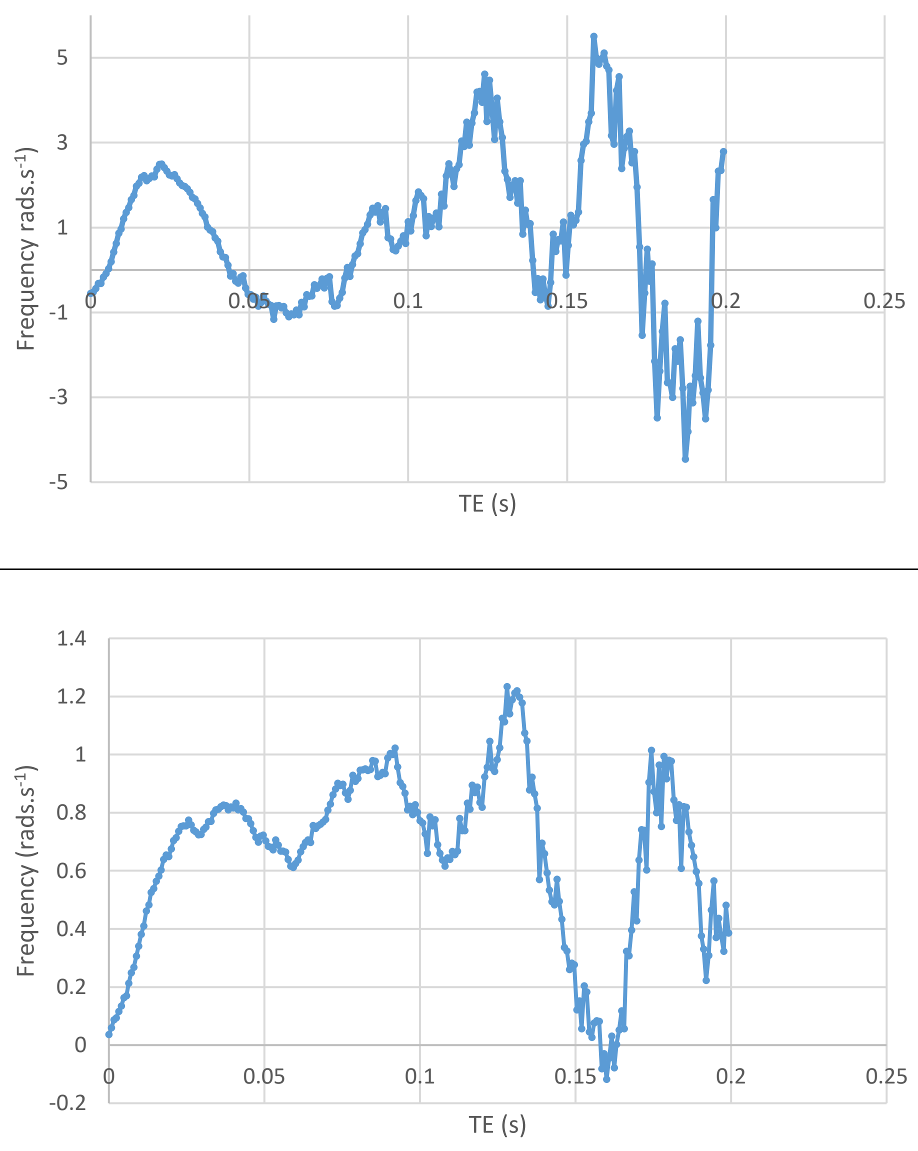

Figure 21. *Frequency measured over time for 10,000 particles diffusing inside a magnetic field. The top graph shows n_D=2 and the lower graph shows n_D=6. χ=2x10^{-7} for both simulations.*

The magnitude of the frequency offset was diminished when the step size increased corresponding to faster diffusion. The signal decayed exponentially over time for both situations however the signal decayed faster as the rate of diffusion decreased.

2.2.3. Discussion

The random walk algorithm successfully modelled diffusion and Brownian motion in 2D. The graph produced (see figure 13) showed the particles starting in the centre of the space and moving outwards over time. This was shown by the Gaussian curve which was fitted to the histogram produced. The standard deviation increased significantly over time as the values of standard deviation increased by 65.2 (±6.5) %. It was found that the random walk algorithm produced an effective diffusion coefficient of 0.5 $(\text{step-size})^2$/timestep, with the standard deviation of the displacement increasing with the square root of time, as expected. Diffusion was successfully modelled as real particles would move randomly backwards and forwards in each dimension and would eventually become evenly distributed throughout the space resulting in a standard deviation which increased over time. This result showed that the model worked as expected and could go on to be used in a diffusion model with confidence that random movement could be emulated.

The log of the signal decreased over time which relates back to a mono-exponential signal decay (1, 5). As a particle experiences spatial displacement due to diffusion it will accumulate a different phase compared to a stationary particle experiencing the same field distribution. A stationary particle will take a set amount of time to accumulate significant phase. Diffusing water particles will move randomly around the magnetic perturber. If the distance moved is similar to the size of the perturber the average field values experienced by the particles will be reduced, thus resulting in slower phase accumulation explaining the reduced signal decay in this simulation. A larger diffusion coefficient (D) would result in the particles moving further over time. The effects due to local structures will be reduced as the particle would move quickly and spend less time in the presence of these structures. As the particle moves around it will sample both positive and negative fields due to the perturber which results in an overall reduction in field intensity being experienced and, as a result, less phase is accumulated and there is a reduced rate of signal decay observed.

The relaxation rate (R_2*) decreased with an increasing size of the diffusion step. This corresponds to R_2* decreasing as the speed of diffusion increases. R_2* has been shown to be a key factor in identifying iron deposits in the brain. Ulla *et al*. (47) have observed that as PD progresses there is an increase in R_2* in the SN and so further investigations into how R_2* is affected by diffusion of particles in the brain will be fundamental in understanding the progression of PD and other similar diseases.

The susceptibility also affected the R_2* value. The higher susceptibilities had a more dramatic decrease in R_2*. Higher susceptibilities provided a larger range of field values experienced by the particles. This allowed for more phase accumulation over the given time frame.

The errors on all of the graphs are not visible due to the errors being very small in comparison to the plotted values. R_2* was calculated using the “linest” function on

Excel, and so the errors associated with this were also given by this function. The errors were very small as there was no direct measurement of external processes and all of the data was created through calculation with well-defined initial parameters.

A significant source of error was due to the limited number of walkers in the simulation and the space they occupied. The number of walkers could not exceed 10,000 as a larger number caused the algorithm to crash or take several hours to run.

There was little optimisation of the code due to time restraints. More work could be done investigating how changes in the mean free path length changes the signal decay. Use of a high powered computer would have also allowed for more testing to fine tune which parameters were to be used in the experiments. Processing times were very long due to the number of perturbers in the simulation and the size of the space used, but step size and time step could have been varied more and the results compared. The results from the simulations at each stage agreed with those found in the literature within the bounds of error (1, 46), and so less time was spent investigating which size of diffusion step provided the best results.

The work in this chapter will be useful in future work as diffusion is important when performing MRI scans of the human body. Diffusion of water molecules can affect the phase difference between neighbouring nuclei (see section 1.2.5) and understanding how parcellation of iron in the brain can affect R_2' and phase is an important factor when studying neurodegenerative disorders. This work could also be extended to compare the data given by the simulation to practical data. Studies could be done on a 7T MRI scanner on phantoms to investigate diffusion using different perturber sizes and the code could be edited to allow for various perturber sizes to be used.

2.3. Conclusion

The aim of the previous experiments was to model the effect of field perturbations due to spherical perturbers on the MR signal evolution and to create a model to simulate diffusion of particles within this magnetic field. In order to achieve these goals, MATLAB R2018a was first used to create an algorithm in which a single spherical perturber was created and the field and signal being produced in the presence of the field perturbation that this sphere produced was generated and recorded. A random walk algorithm was constructed and tested in order to ensure diffusing particles could be mimicked accurately. The random walk algorithm was then integrated into a new program which consisted of many perturbers diffusing in a magnetic field distribution produced by a random distribution of spherical perturbers with low volume fraction. The signal and phase data from this new model was saved to an Excel spreadsheet and analysed.

An image of the field produced by the single sphere was successfully generated. The image showed the expected dipolar form of the field perturbation and a signal was obtained which showed an exponential decay. It was seen that the intensity and frequency of the detected signal changed with susceptibility. The signal decay was the fastest when larger magnetic susceptibilities were used. The volume fraction was varied in order to see if this would change the relaxation and the frequency of the signal. The volume fraction was initially 1×10^{-6} and was then multiplied by a factor of 8. As a result of this, the frequency increased by a factor of ~ 8. The simulated data agreed with the literature values within a reasonable margin of error and therefore suggests that the static dephasing regime can be simulated for a single spherical perturber. When 10,000 multiple stationary perturbers were added, it was seen that R2* increased.

The random walk algorithm successfully modelled diffusing particles in 2D and was later used in 3D in the diffusion model. The standard deviation of the particles increased over time and it was seen that there was a positive linear relationship between σ^2 and time which agreed with the theory (46).

When looking at diffusing particles, it was seen that the log of the signal decreased over time, but only decreased linearly after 0.05s. When looking at stationary particles, the expected signal decay follows an exponential relationship which was described by equation 24, but when these particles start to move they experience spatially varying magnetic fields and so take time to accumulate phase. R_2^* was calculated from the linear sections of the graphs. The R_2^* times decreased with increasing diffusion steps and also increased with larger susceptibility values.

Future work could be done by investigating a wider range of magnetic susceptibilities for all of the situations discussed above. The size of the space that the simulations were carried out in was limited by computer processing power and time restraints and so further work could be done evaluating how signal and phase evolution varies with diffusion rates over larger volumes. More perturbers could also be added into the simulation if a more powerful computer was available. Software could be developed which would analyse MRI data of phantoms to see if there are in fact any noticeable discrepancies in R_2^* and signal data between voxels in situations with different numbers of magnetic perturbers and diffusion speeds to see if the results agree with the work done in this thesis. This work could also be extended for use in creating more accurate QSM maps. Fully understanding how magnetic perturbers found in the brain can cause phase variations will allow for more accurate mapping technologies which can then be used in Alzheimer's research.

3. Pilot Study of measurement of susceptibility maps in early AD patients at 7T.

Contents

This chapter described the initial work done to test the feasibility of scanning AD patients with a 7T Philips MRI scanner. As part of a pilot study, phase images obtained using a high-resolution gradient echo scan are analysed using quantitative susceptibility mapping software.

3.1. Introduction

The UK7T Network (48) was established in 2016 by five universities; the University of Nottingham, University of Oxford, Cardiff University, University of Cambridge and the University of Glasgow. One of the aims of the network was to establish uniform neuroimaging protocols on 7T scanners across the different universities. This work was crucial as it ensures that any data collected across the sites could be shared and consistently analysed. Good harmonisation of scanning techniques on all of the 7T scanners, which included three different types of system (Philips Achieva, Siemens Magnetom and Siemens Terra) was achieved. A "travelling head" study, in which the same 10 subjects have been scanned at all of the sites is underway. The data collected from these scans will be used to validate the effectiveness of the harmonisation. The harmonised imaging sequences are now being applied to a smaller cohort (five per site) of patients with early Alzheimer's disease (AD) in a pilot study. In particular high-resolution gradient echo (GE) images were acquired and this chapter focuses on the generation of quantitative susceptibility maps from these data.

3.2. Method

A Philips 7T Achieva MRI scanner was used to scan three patients who suffered from AD with mild cognitive impairment. Patients were invited to take part in this study after a consultation with a neurology specialist at the hospital where they are normally treated. They were provided with a description of the study and information about MRI procedures. They were then given a consent form which was signed by both the participant and the investigator who was taking consent. As part of the scanning session a 3D GE scan was acquired using a Nova 2Tx/32Rx coil with 0.7 mm isotropic resolution, 224 x 224 x 224 mm^3 field of view, TR=31 ms, TE=20 ms. SENSE factor 2 x 2, 70 Hz bandwidth, and 15° flip angle.

A high powered computer was used to process the images using QSM box (21) as a standard computer did not have enough memory and CPU power to run the program. This software uses MSDI (see section 1.2.3) to produce quantitative susceptibility maps of the imaged brains. MATLAB R2013 was used to run QSM box as this was the most modern version of MATLAB available on the computer.

QSM box (21) took magnitude and phase MRI data in the form of a NIFTI files along with a file detailing the parameters of the scan, i.e. TE, field direction [0 1 0] and resolution [0.7 0.7 0.7] mm^3 and used them to generate quantitative susceptibility maps. These maps were then opened using MATLAB R2019 (Mathworks, MA, USA) and colour bars were added.

3.3. Results

Example magnitude images and corresponding QSM maps can be seen in figures 22 and 23. The coronal, axial and sagittal slices shown in these images were chosen as they gave the best view of the hippocampus.

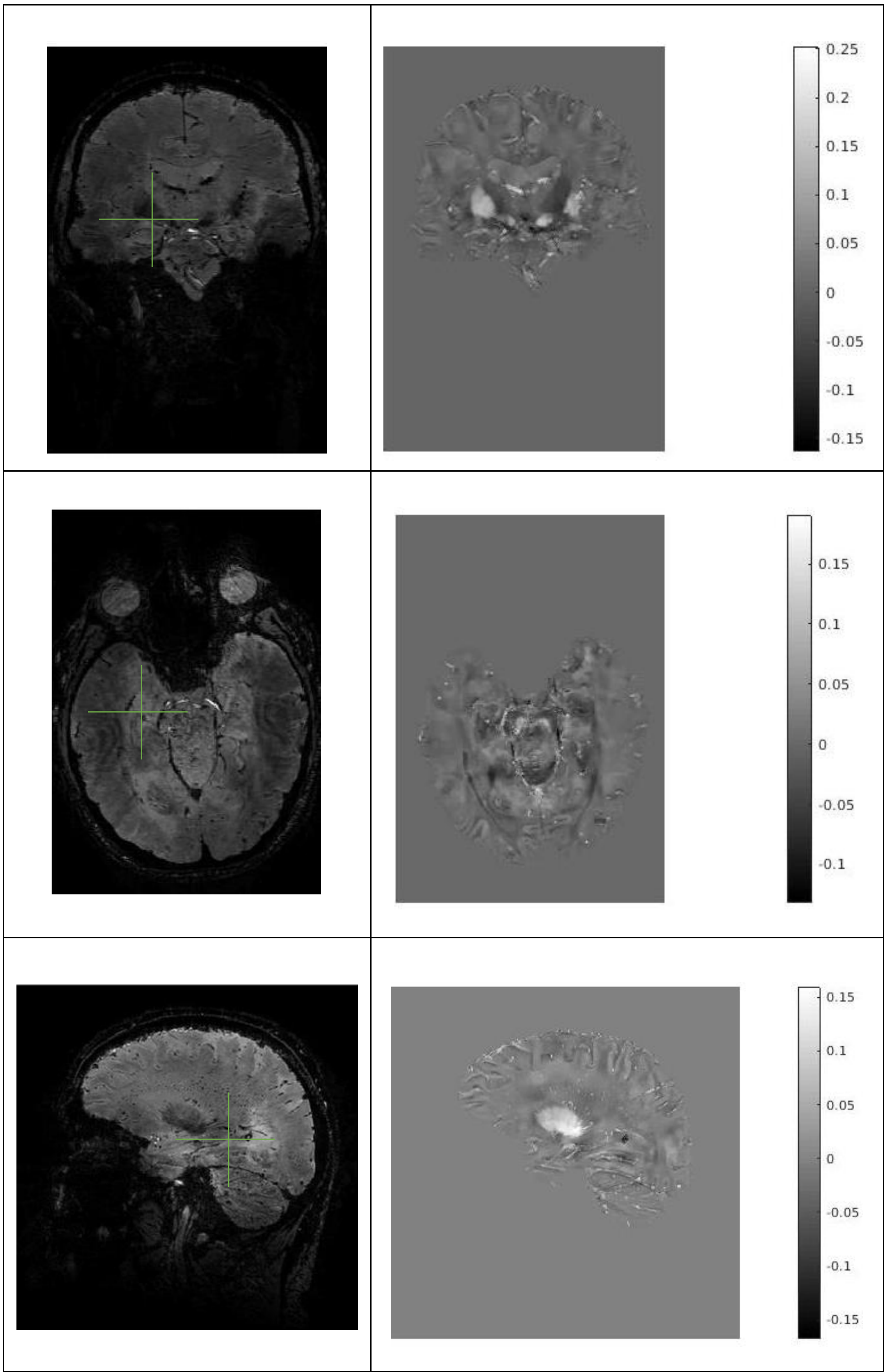

Figure 22. *Magnitude images (left) and corresponding QSM maps (right) of the first AD patient. Colour bars show pixel intensity for the susceptiblity maps in parts per million. Green crosses show the location of the hippocampus*

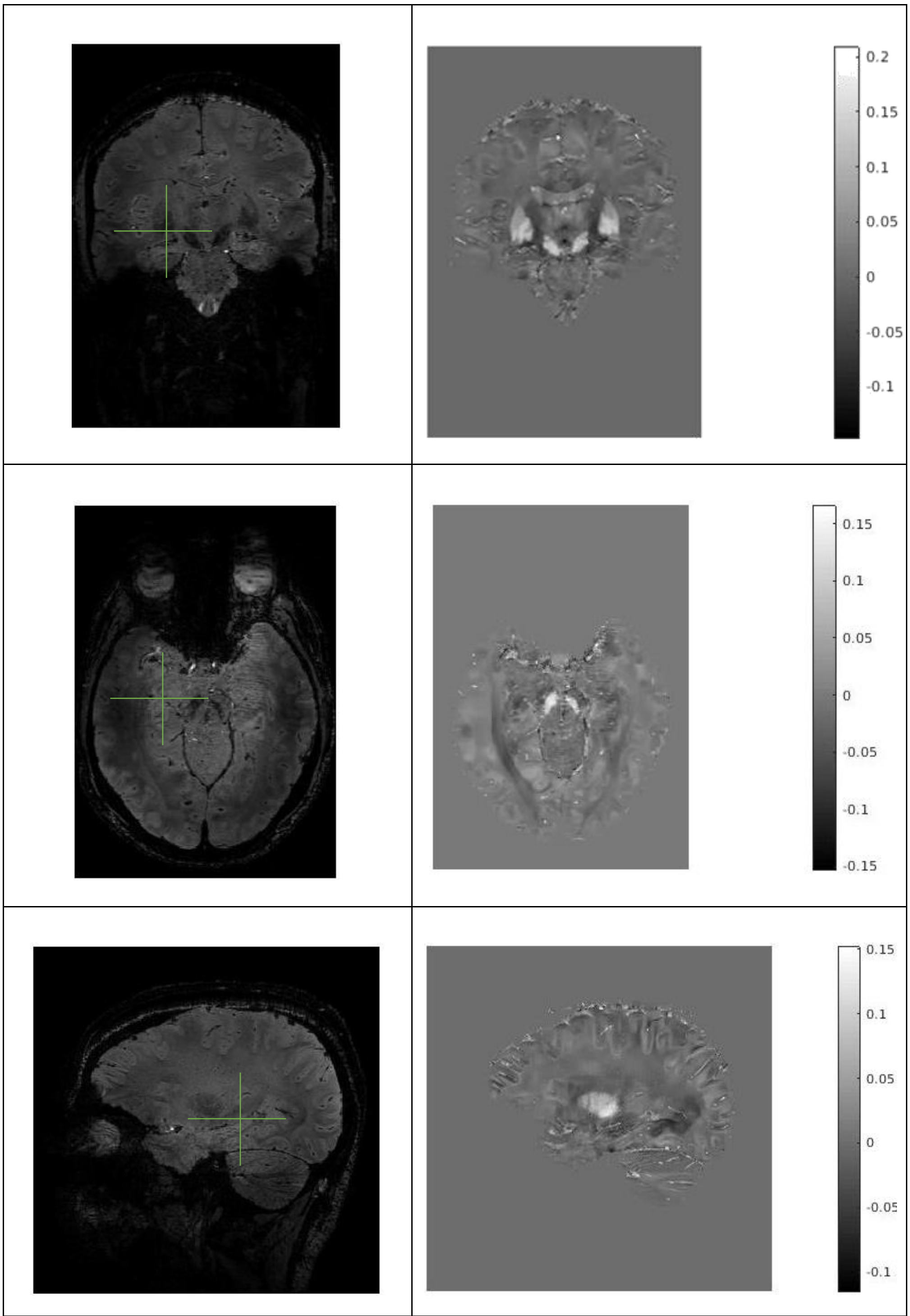

Figure 23. *Magnitude images (left) and corresponding QSM maps (right) of the second AD patient. Colour bars show pixel intensity for the susceptiblity maps in parts per million.*

The areas marked by the green crosses in figure 22 show the hippocampus. Zoomed in images of these areas can be seen in figure 24.

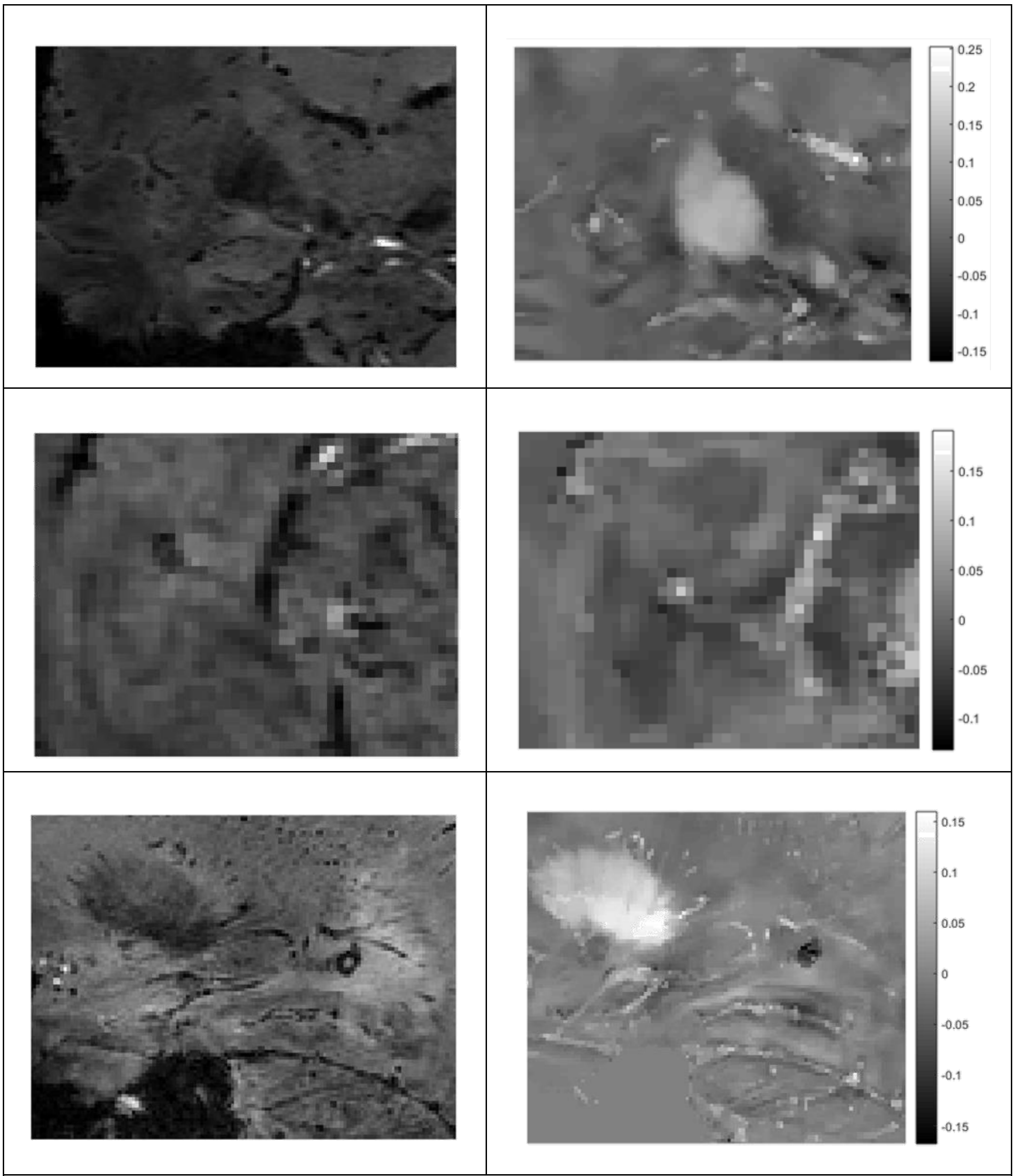

Figure 24. *Close up images showing the hippocampus of the first patient. Magnitude images are on the left, and susceptibility maps are on the right. Colour bars show the susceptibility in parts per million. Images shown are in the coronal, axial and sagittal plane respectively.*

The data from two of the patients (see figures 22 and 23) showed a clear image of the brain and susceptibility maps which highlighted the various susceptibilities throughout the brain. The third patient however moved whilst the scans were being performed and as a result the magnitude images show noticeable movement artefacts. The QSM maps which came from these images do not appear to show any artefacts which are as serious as in the magnitude images (see figure 25).

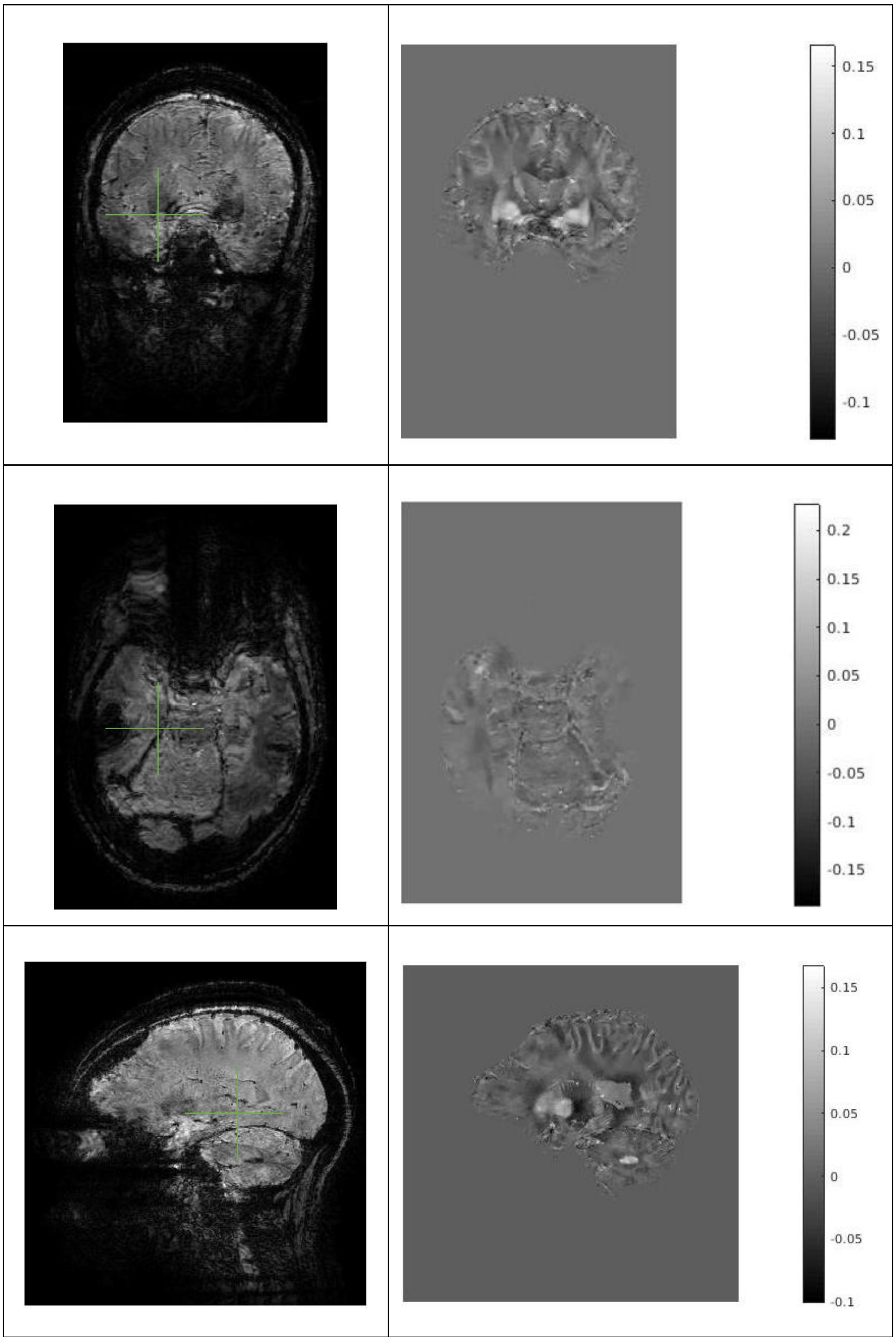

Figure 25. *The AD patient moved whilst in the scanner causing the magnitude images (left) to blur but the corresponding QSM maps (right) do not show the blurring.*

3.4. Discussion

The results indicate that images with a high signal to noise ratio can be obtained from high resolution GE scans acquired from subjects with early AD at 7T. These images can be then used to make quantitative susceptibility maps which show a high contrast between areas of high and low magnetic susceptibilities. With a 12-minute acquisition time, it is difficult for subjects to remain still throughout the scan, and the magnitude data in one of the three subjects scanned showed evident effects of head movement. The QSM data generated from all three subjects was however of good quality. The depiction of the hippocampus was clear in the QSM and magnitude data based the known anatomical features of this structure. In future work it should be possible to quantify the susceptibility values in different hippocampal sub-structures.

The brain starts to deteriorate when a person suffers from AD. The breakdown of the myelinated sheathes associated with neurons and the formation of senile plaques in the hippocampus means that the iron which has previously been in an unreactive state is able to cause redox reactions and therefore can lead to oxidative stress on cells. It has already been seen (37) that there is higher levels of iron in the hippocampus in AD patients than there is in healthy controls.

The decline of cognitive functions as AD progresses may cause problems when scanning patients. The third patient moved slightly whilst in the scanner. All patients were able to give their own consent to go into the scanner, but future work may use more severely impaired patients. Whilst in the scanner patients could become confused and their ability to lie still may be inhibited. It is reasonable to try and keep the patient in the scanner for as little time as possible in order to prevent any distress which may arise from being in a loud and cramped environment. Blurry scans will lead to inaccurate QSM data, however bringing the patient back to be rescanned is far from ideal. Motion correction techniques will need to be considered or developed when undergoing future scans so that the patient will not need multiple lengthy sessions.

This work could be continued by looking at more AD patients. Analysing data from healthy aged matched controls would be fundamental when trying to determine if there is a difference in susceptibility in the hippocampus when a patient has AD. Now that the UK7T study has helped to develop standard protocols which can be used across many scanners, there is opportunity for collaboration between universities which in turn will allow for larger studies as the capture area for potential patients will be much larger and scanning centres will be more easily accessible for patients, reducing the need for them to travel as far.

4. Summary

Last year 850,000 people in the UK alone were suffering from AD or a form of dementia. The homeostasis of iron is affected and the breakdown of myelin and the formation of senile plaques results in increasing iron levels. Increased iron levels in the hippocampus causes the formation of free radicals and oxidative stress to cells (37). QSM can be used to assess the structural changes in the hippocampus by monitoring the changing magnetic susceptibility due to increased iron levels as the disease progresses (38). Spatially varying inhomogeneity in magnetic fields causes a dephasing in MR signal and this can be a result of diffusion (1). Understanding diffusion in various situations is important when analysing QSM maps and so designing a model which can simulate diffusion in a magnetic field is useful.

The aim of this work was to develop software which could accurately model diffusing particles in a magnetic field and to also use QSM box (21) to look at the hippocampus of patients with AD.

An algorithm was created using MATLAB R2018a to model a single stationary dipole. This was achieved by designing a spherical space with a volume magnetic susceptibility of $\chi = 1\times10^{-6}$, $\gamma=267.5\times10^{6}$ rads·s·T^{-1} and field strength of 7T and placing a dipole inside. The spatially varying field perturbation due to the dipole was calculated along with the resulting phase offset. This produced images which successfully showed the field and phase. When different susceptibilities were used it was seen that the signal decayed faster when smaller susceptibilities were used. Susceptibility values were 2.0×10^{-4}, 4.0×10^{-4} and 8.0×10^{-4}.When lower susceptibilities were used there was less magnetisation and so the time taken for the nuclear spin to relax was shorter. The simulation was run again but in order to test if volume fraction was directly related to frequency the volume fraction was reduced by a factor of 8 this caused the frequency to increase by a factor of 7.88434(±0.00024). R_2* was proportional to volume fraction for every susceptibility value used.

R_2' and $\Delta\omega$ were calculated and a plot of these against $\gamma\chi B_0$ VF was created. This gave a gradient which could be compared to the literature (1) to assess if the simulation agreed with the static dephasing regime. The accuracy of the phase data was accurate to within 6% and the signal data was within 0.6% of the literature value. This showed that the static dephasing regime applied to the scenario defined by the model.

A random walk algorithm was created in order to model diffusion. This was achieved using 1×10^{5} particles and 100 time steps with a jump size of 1. The position of the particles after a given time was found by creating a histogram which showed the root mean squared displacement of the particles. The algorithm successfully modelled diffusion as it was seen that there was a linear relationship between σ^2 and time. The model was edited to allow the random walk to move in 3D and was integrated into the dipole simulation. The model used 10,000 perturbers which all moved a set distance with each time step. This distance was increased and R_2* was calculated for each scenario. R_2* decreased with an increasing diffusion step due to the perturber size becoming comparable to the size of the diffusion step. There is a slower phase evolution due to the range of phase values the particles experience being reduced due to diffusion.

GRE scans were taken of three AD patients who suffered from mild cognitive impairment using a Philips 7T Achieva MRI scanner and a Nova 2Tx/32Rx coil. QSM box was run on the data which created susceptibility maps of the brain and slices which showed the hippocampus was selected. Motion artefacts were seen as it was difficult for the patients to lie still whilst the scans were being undertaken, however, the resulting data was still clear and was able to be used to create QSM maps. Knowledge of the anatomical structure of the brain confirmed that the hippocampus was shown clearly in both the images and the QSM maps.

This work has successfully managed to produce a model which can model the static dephasing regime for a singular dipole and has also created an algorithm which can model diffusing particles in a magnetic field. Three AD patients were scanned and QSM maps were successfully created from the resulting data. Some future work would be to add more perturbers and more loop iterations to the model and adding some barriers to simulate blood vessels and different parts of the brain. More AD patients should be scanned and their data should be analysed to increase the sample size looked at in this work. The data from healthy controls should also be analysed and used as a comparison to the AD data. Fast sequences should be used in scans in order to keep the patient comfortable and still to try and avoid motion artefacts. Sub structures of the hippocampus could be investigated and quantitative susceptibility maps could be generated. Collaborations between more facilities with 7T MRI scanners would also allow for data to be collected in other parts of the country and across the globe and so patients will have easier access to research centres

5. References

1. Yablonskiy, D. and Haacke, E. (1994). Theory of NMR signal behavior in magnetically inhomogeneous tissues: The static dephasing regime. *Magnetic Resonance in Medicine*, 32(6), pp.749-763.
2. Dementia Statistics Hub. (2019). *Numbers of people in the UK | Dementia Statistics Hub*. [online] Available at: https://www.dementiastatistics.org/statistics/numbers-of-people-in-the-uk/ [Accessed 6 Sep. 2019].
3. Alzheimer's Disease and Dementia. (2019). *Facts and Figures*. [online] Available at: https://www.alz.org/alzheimers-dementia/facts-figures [Accessed 6 Sep. 2019].
4. nhs.uk. (2018). *Alzheimer's disease - Diagnosis*. [online] Available at: https://www.nhs.uk/conditions/alzheimers-disease/diagnosis/ [Accessed 25 Jul. 2019].
5. McRobbie, D., Moore, E. and Graves, M. (2006). *MRI from picture to proton*. 2nd ed. New York: Cambridge University Press, pp.30-42, 137-166.
6. Young, H. (2014). *Sears and Zemansky's university physics with modern physics Technology update*. Essex: Pearson Education, pp.1585-1592.
7. Brown, R., Norman Cheng, Y., Haacke, E., Thompson, M. and Venkatesan, R. (2014). *Magnetic Resonance Imaging: Physical Principles and Sequence Design*. 2nd ed. Hoboken: John Wiley & Sons.
8. Zecca, L., Tampellini, D., Gerlach, M., Riederer, P., Fariello, R. and Sulzer, D. (2001). Substantia nigra neuromelanin: structure, synthesis, and molecular behaviour. *Journal of Clinical Pathology*, 54(6), pp.414-418.
9. Chavhan, G., Babyn, P., Thomas, B., Shroff, M. and Haacke, E. (2009). Principles, Techniques, and Applications of T2*-based MR Imaging and Its Special Applications. *RadioGraphics*, 29(5), pp.1433-1449.
10. Kingsley, P. (1999). Methods of measuring spin-lattice (T1) relaxation times: An annotated bibliography. *Concepts in Magnetic Resonance*, 11(4), pp.243-276.
11. Jones, J. and Bell, D. (2019). *T1 relaxation time | Radiology Reference Article | Radiopaedia.org*. [online] Radiopaedia.org. Available at: https://radiopaedia.org/articles/t1-relaxation-time?lang=gb [Accessed 21 Oct. 2019].
12. Jones, J. and Bell, D. (2019). *T1 weighted image | Radiology Reference Article | Radiopaedia.org*. [online] Radiopaedia.org. Available at: https://radiopaedia.org/articles/t1-weighted-image?lang=gb [Accessed 21 Oct. 2019].
13. Wager, T. and Lindquist, M., 2015. *Principles Of Fmri*. [ebook] Leanpub. Available at: <https://leanpub.com/principlesoffmri> [Accessed 9 March 2020].

14. Acosta-Cabronero, J., Williams, G., Cardenas-Blanco, A., Arnold, R., Lupson, V. and Nestor, P. (2013). In Vivo Quantitative Susceptibility Mapping (QSM) in Alzheimer's Disease. *PLoS ONE*, 8(11), p.e81093. https://journals.plos.org/plosone/article?id=10.1371/journal.pone.0081093#s5
15. Nde-ed.org. (2019). *Magnetic Materials*. [online] Available at: https://www.nde-ed.org/EducationResources/CommunityCollege/MagParticle/Physics/MagneticMatls.htm [Accessed 3 Jul. 2019].
16. Langkammer, C., Schweser, F., Krebs, N., Deistung, A., Goessler, W., Scheurer, E., Sommer, K., Reishofer, G., Yen, K., Fazekas, F., Ropele, S. and Reichenbach, J. (2012). Quantitative susceptibility mapping (QSM) as a means to measure brain iron? A post mortem validation study. *NeuroImage*, 62(3), pp.1593-1599.
17. Haacke, E., Liu, S., Buch, S., Zheng, W., Wu, D. and Ye, Y. (2015). Quantitative susceptibility mapping: current status and future directions. *Magnetic Resonance Imaging*, 33(1), pp.1-25.
18. Li, L. (2001). Magnetic susceptibility quantification for arbitrarily shaped objects in inhomogeneous fields. *Magnetic Resonance in Medicine*, 46(5), pp.907-916.
19. Schweser, F., Robinson, S., de Rochefort, L., Li, W. and Bredies, K. (2016). An illustrated comparison of processing methods for phase MRI and QSM: removal of background field contributions from sources outside the region of interest. *NMR in Biomedicine*, 30(4), p.e3604.
20. A robust multi-scale approach to quantitative susceptibility mapping. (2018). *NeuroImage*, 183, pp.7-24.
21. Acosta-Cabronero, J. (2018). *QSM box*. Welcome Centre for Human Neuroimaging, University College London.
22. Sukstanskii, A. and Yablonskiy, D. (2001). Theory of FID NMR Signal Dephasing Induced by Mesoscopic Magnetic Field Inhomogeneities in Biological Systems. *Journal of Magnetic Resonance*, 151(1), pp.107-117.
23. Tuch, D., Reese, T., Wiegell, M. and Van J. Wedeen (2003). Diffusion MRI of Complex Neural Architecture. *Neuron*, 40(5), pp.885-895.
24. Le Bihan, D. and Iima, M. (2015). Diffusion Magnetic Resonance Imaging: What Water Tells Us about Biological Tissues. *PLOS Biology*, 13(9).
25. Le Bihan, D. (2007). The ‘wet mind’: water and functional neuroimaging. *Physics in Medicine and Biology*, [online] 52(7). Available at: https://iopscience.iop.org/article/10.1088/0031-9155/52/7/R02 [Accessed 22 Jul. 2019].
26. Jahng, G., Li, K., Ostergaard, L. and Calamante, F., 2014. Perfusion Magnetic Resonance Imaging: A Comprehensive Update on Principles and Techniques. *Korean Journal of Radiology*, 15(5), p.554.
27. Piñero, D. and Connor, J. (2000). Iron in the Brain: An Important Contributor in Normal and Diseased States. *The Neuroscientist*, 6(6), pp.435-453.

28. Rouault, T. and Cooperman, S. (2006). Brain Iron Metabolism. *Seminars in Pediatric Neurology*, 13(3), pp.142-148.
29. Schneider, S. and Bhatia, K. (2012). Excess iron harms the brain: the syndromes of neurodegeneration with brain iron accumulation (NBIA). *Journal of Neural Transmission*, 120(4), pp.695-703.
30. Sternberg, Z., Hu, Z., Sternberg, D., Waseh, S., Quinn, J., Wild, K., Jeffrey, K., Zhao, L. and Garrick, M. (2017). Serum Hepcidin Levels, Iron Dyshomeostasis and Cognitive Loss in Alzheimer’s Disease. *Aging and Disease*, 8(2), p.215.
31. Haacke, E., Cheng, N., House, M., Liu, Q., Neelavalli, J., Ogg, R., Khan, A., Ayaz, M., Kirsch, W. and Obenaus, A. (2005). Imaging iron stores in the brain using magnetic resonance imaging. *Magnetic Resonance Imaging*, 23(1), pp.1-25.
32. Knovich, M., Storey, J., Coffman, L., Torti, S. and Torti, F. (2009). Ferritin for the clinician. *Blood Reviews*, 23(3), pp.95-104.
33. Theil, E. (1987). Ferritin: Structure, Gene Regulation, And Cellular Function In Animals, Plants, And Microorganisms. *Annual Review of Biochemistry*, 56(1), pp.289-315.
34. Ward, A., Caro, J., Getsios, D., Ishak, K., O'Brien, J. and Bullock, R. (2003). Assessment of health economics in Alzheimer's disease (AHEAD): treatment with galantamine in the UK. *International Journal of Geriatric Psychiatry*, 18(8), pp.740-747.
35. nhs.uk. (2018). *Alzheimer's disease - Diagnosis*. [online] Available at: https://www.nhs.uk/conditions/alzheimers-disease/diagnosis/ [Accessed 25 Jul. 2019].
36. Ayton, S., Faux, N. and Bush, A. (2015). Ferritin levels in the cerebrospinal fluid predict Alzheimer’s disease outcomes and are regulated by APOE. *Nature Communications*, 6(1).
37. Smith, M., Harris, P., Sayre, L. and Perry, G. (1997). Iron accumulation in Alzheimer disease is a source of redox-generated free radicals. *Proceedings of the National Academy of Sciences*, 94(18), pp.9866-9868.
38. Antharam, V., Collingwood, J., Bullivant, J., Davidson, M., Chandra, S., Mikhaylova, A., Finnegan, M., Batich, C., Forder, J. and Dobson, J. (2012). High field magnetic resonance microscopy of the human hippocampus in Alzheimer's disease: Quantitative imaging and correlation with iron. *NeuroImage*, 59(2), pp.1249-1260.
39. Haeger, A., Costa, A., Schulz, J. and Reetz, K. (2019). Cerebral changes improved by physical activity during cognitive decline: A systematic review on MRI studies. *NeuroImage: Clinical*, 23, p.101933.
40. Wakamatsu, K., Fujikawa, K., Zucca, F., Zecca, L. and Ito, S. (2003). The structure of neuromelanin as studied by chemical degradative methods. *Journal of Neurochemistry*, 86(4), pp.1015-1023.
41. Zecca, L., Casella, L., Albertini, A., Bellei, C., Zucca, F., Engelen, M., Zadlo, A., Szewczyk, G., Zareba, M. and Sarna, T. (2008). Neuromelanin can protect against iron mediated oxidated damage in system modelling iron overload of brain aging and Parkinson’s disease. *Journal of Neurochemistry*.

42. Sulzer, D., Cassidy, C., Horga, G., Kang, U., Fahn, S., Casella, L., Pezzoli, G., Langley, J., Hu, X., Zucca, F., Isaias, I. and Zecca, L. (2018). Neuromelanin detection by magnetic resonance imaging (MRI) and its promise as a biomarker for Parkinson’s disease. *npj Parkinson's Disease*, 4(1).
43. Lee, H., Baek, S., Chun, S., Lee, J. and Cho, H. (2018). Specific visualization of neuromelanin-iron complex and ferric iron in the human post-mortem substantia nigra using MR relaxometry at 7T. *NeuroImage*, 172, pp.874-885.
44. Prasad, S., Stezin, A., Lenka, A., George, L., Saini, J., Yadav, R. and Pal, P. (2018). Three-dimensional neuromelanin-sensitive magnetic resonance imaging of the substantia nigra in Parkinson's disease. *European Journal of Neurology*, 25(4), pp.680-686.
45. Sasaki, M., Shibata, E., Tohyama, K., Takahashi, J., Otsuka, K., Tsuchiya, K., Takahashi, S., Ehara, S., Terayama, Y. and Sakai, A. (2006). Neuromelanin magnetic resonance imaging of locus ceruleus and substantia nigra in Parkinson's disease. *NeuroReport*, 17(11), pp.1215-1218.
46. Meerschaert, M. and Sikorskii, A. (2012). *Stochastic models for fractional calculus*. Berlin: De Gruyter, pp.117-118.
47. Ulla, M., Bonny, J., Ouchchane, L., Rieu, I., Claise, B. and Durif, F. (2013). Is R2* a New MRI Biomarker for the Progression of Parkinson’s Disease? A Longitudinal Follow-Up. *PLoS ONE*, 8(3), p.e57904.
48. Clarke, W., Mougin, O., Driver, I., Rua, C., Morgan, A., Asghar, M., Clare, S., Francis, S., Wise, R., Rodgers, C., Carpenter, A., Muir, K. and Bowtell, R. (2019). Multi-site harmonization of 7 Tesla MRI neuroimaging protocols. *NeuroImage*, p.116335

6. Appendix

Contents

6.1. Appendix 1

This appendix contains the MATLAB codes used to produce the results of this thesis.

Stationary Dipole Simulation

Define an array

```
x=[-100:100];
y=[-100:100];
z=[-100:100];

[X,Y,Z]=meshgrid(x,x,x);
```

Define spherical coordinate/array

```
r=sqrt(X.^2+Y.^2+Z.^2);
```

Calculate form of dipole field

```
Suscep = input('input susceptibility value');
V=input('input volume of sphere to be considered in microns');
B0=input('input B0 field strength');

Bz=((Suscep.*V.*B0)./(4*pi)).*((3*Z.^2./r.^2)-1)./(r.^3);
```

Sort out divergance at centre

```
Bz(isnan(Bz))=0;
Bz(isinf(Bz))=0;
```

Create figure of field in X=0 plane.

```
figure('Name','Field map')
```

Phase offset

```
gamma=275.5e6;
tau=input('input a time value');

phase=gamma*tau.*Bz;
imagesc(squeeze(phase(101,:,:)))
maskphase=mask.*phase;
imagesc(squeeze(maskphase(101,:,:)))
colorbar
xlabel('voxel (a.u)')
ylabel('voxel (a.u)')
```

Plot the phase shift along the X=0 dimension*. X axis has values on up to 201 as thats how many columns there are.*

```
line_phase=squeeze(phase(101,:,:));
plotphase=squeeze(line_phase(101,:));
figure
    plot(plotphase)
```

Simulate signal

```
S=exp(i.*phase);

real_S=real(S);
realplot=mask.*real_S;
imagereal=squeeze(realplot(101,:,:));

figure('Name','Real signal')
    imagesc(imagereal)
    colorbar

figure('Name','Graph real signal')
    plot(squeeze(imagereal(101,:)))
```

Plot imaginary parts

```
imag_S=imag(S);
imagplot=mask.*imag_S;
imag_image=squeeze(imagplot(101,:,:));

figure('Name','Imaginary signal')
    imagesc(imag_image)
    colorbar

figure('Name','Graph imaginary plot')
    plot(squeeze(imag_image(101,:)))
```

Magnitude of the signal changes over time

Sum across the voxels, and this will include both real and imaginary parts of the signal.

```
count=1;
tau=0;
time=zeros(1,1000);
Sig_tot=zeros(1,1000);

for count=1:100

    phase=gamma*tau.*Bz;
    S=exp(1i*phase);
    S(101,101,101)=0;
    Stot=sum(sum(sum(S)));
    Sig_tot(count)=Stot;
    tau=tau+(10);
    time(count)=tau;

end

abs(Sig_tot);
plot(time,Sig_tot, '.');

title('Plot of signal and time')
xlabel('time (s)')
ylabel('Signal (a.u)')
```

map phase(angle) over time

```
phaseangle=angle(Sig_tot);
plot(time,phaseangle)
title('Phase plot using angle funciton')
xlabel('time')
ylabel('phase angle')
```

How does the decay vary with susceptibiliy:

```
x=[-100:100];
y=[-100:100];
z=[-100:100];

[X,Y,Z]=meshgrid(x,x,x);
r=sqrt(X.^2+Y.^2+Z.^2);

susceparray=input('input three suscep values in 1D array form');
B0=input('input field strength in T ');
V=input(' input volume in microns ');
gamma=275.5e6;

count=1;
tau=0
time=zeros(1,100);
Sig_tot1=zeros(1,100);
Sig_tot2=zeros(1,100);
Sig_tot3=zeros(1,100);
phaseangle1=zeros(1,100);
phaseangle2=zeros(1,100);
phaseangle3=zeros(1,100);

Sus_val_1=susceparray(1);
Sus_val_2=susceparray(2);
Sus_val_3=susceparray(3);
```

```
Bz1=((Sus_val_1.*V.*B0)./(4*pi)).*((3*Z.^2./r.^2)-1)./(r.^3);
Bz2=((Sus_val_2.*V.*B0)./(4*pi)).*((3*Z.^2./r.^2)-1)./(r.^3);
Bz3=((Sus_val_3.*V.*B0)./(4*pi)).*((3*Z.^2./r.^2)-1)./(r.^3);

Bz1(isnan(Bz1))=0;
Bz1(isinf(Bz1))=0;

Bz2(isnan(Bz2))=0;
Bz2(isinf(Bz2))=0;

Bz3(isnan(Bz3))=0;
Bz3(isinf(Bz3))=0;

for count=1:100

    phase1=gamma.*Bz1.*tau;
    S1=exp(1i.*phase1);
    S1(101,101,101)=0;
    Stot1=sum(sum(sum(S1)));
    Sig_tot1(count)=Stot1;


    phase2=gamma.*Bz2.*tau;
    S2=exp(1i.*phase2);
    S2(101,101,101)=0;
    Stot2=sum(sum(sum(S2)));
    Sig_tot2(count)=Stot2;
```

```
    phase3=gamma.*Bz3.*tau;
    S3=exp(1i.*phase3);
    S3(101,101,101)=0;
    Stot3=sum(sum(sum(S3)));
    Sig_tot3(count)=Stot3;


    time(count)=tau;
    tau=tau+100e-3;
    count=count+1;

end

Sig_tot_1= abs(Sig_tot1);
Sig_tot_2=abs(Sig_tot2);
Sig_tot_3=abs(Sig_tot3);

figure ('Name' , 'Graph of signal for various susceptibilities ');


plot(time,Sig_tot_1,'*')
hold on
plot(time,Sig_tot_2,'o')
hold on
plot(time, Sig_tot_3, '-')
hold off
```

```
label1=num2str(susceparray(1));
label2=num2str(susceparray(2));
label3=num2str(susceparray(3));
legend(label1, label2, label3)
xlabel('Time (s)')
ylabel('Signal intensity (a.u)')


figure ('Name', 'Graph of phase angles');

phaseangle1=angle(Sig_tot1);
plot(time, phaseangle1, '*')
hold on
phaseangle2=angle(Sig_tot2);
plot(time, phaseangle2, 'o')
hold on
phaseangle3=angle(Sig_tot3);
plot(time, Sig_tot3, '-')
hold off
legend(label1, label2, label3)
xlabel('Time, (s)')
ylabel('Phase, (rads)' )
```

```
figure ('Name', 'gradient of phase');
grad1=diff(phaseangle1);
plot(time(2:end), grad1)
hold on
grad2=diff(phaseangle2);
plot(time(2:end), grad2)
hold on
grad3=diff(phaseangle3);
plot(time(2:end), grad3)
hold off
legend(label1, label2, label3)
xlabel('Time(s)')
ylabel('gradient of phase')
```

```
figure
freq2=grad2/1e-3;
plot(time(2:end), freq2)
hold on
freq3=grad3/1e-3;
plot(time(2:end), freq3)
hold off
legend(label2, label3) %label1 omitted as only plotting smaller susceps
xlabel('Time (s)')
ylabel('Frequency (Hz)')

figure('Name', 'slope of ln(mag) vs time')
log_2=log(Sig_tot_2);
slope_log_2=diff(log_2)/1e-3;
plot(time(2:end), slope_log_2)
hold on
log_3=log(Sig_tot_3);
slope_log_3=diff(log_3)/1e-3;
plot(time(2:end), slope_log_3)
hold off
xlabel('Time (s)')
ylabel('gradient of magnitude of signal')

timeplot=time(2:end);
```

Random Walk

```
X=zeros(1,100); %X is array after 1st timestep
start=0;

for N=1:100  % N is number of particles

    r=randn(1,1);
    X(N)= start+r;
    N=N+1;

end

figure('Name', 'position after 1 timestep')
histfit(X)
xlabel('distance moved from origin')
ylabel('number of particles at position')

X_T=X.'; %transpose data so it can be used in fitdist
fitX=fitdist(X_T, 'Normal') % analysis after 1 timestep

i=1; %loop counter
Xt=X; %makes a new array so the old one can be kept for plotting later

for t=1:10 %do 10 time steps

for i=1:100 %loop this 100 times as there are 100 particles

    start_X=Xt(i); %get position
    r2=randn(1);
    Xt(i)=start_X+r2; %store position after moving distance 'r'
    i=i+1; %loop counter

end
```

```
for i=1:100 %loop this 100 times as there are 100 particles

    start_X=Xt(i); %get position
    r2=randn(1);
    Xt(i)=start_X+r2; %store position after moving distance 'r'
    i=i+1; %loop counter

end

%plot graph after each timestep
figure
histfit(Xt);
xlabel('distance moved from origin')
ylabel('number of particles at position')
X2_T=Xt.';
fitX2=fitdist(X2_T,'Normal')

end

figure('Name', 'Both histograms')
h=histfit(X);
alpha(0.5)
h(2).Color=[.2 .2 .2];
hold on
H=histfit(Xt);
alpha(0.5)
legend('timestep 1', 'timestep 1', 'timestep 10', 'timestep 10')
xlabel('distance moved from origin')
ylabel('number of particles at position')
```

Isofield calculation

```
function [fieldshift] = isofieldcalc(suscep,voxdim,B0unit)

dims=size(suscep);

kx=fftshift((-dims(1)/2):(dims(1)/2-1));
ky=fftshift((-dims(2)/2):(dims(2)/2-1));
kz=fftshift((-dims(3)/2):(dims(3)/2-1));
kxmat=repmat(reshape(kx,[dims(1) 1 1]),[1 dims(2) dims(3)])/dims(1)/voxdim(1);
kymat=repmat(reshape(ky,[1 dims(2) 1]),[dims(1) 1 dims(3)])/dims(2)/voxdim(2);
kzmat=repmat(reshape(kz,[1 1 dims(3)]),[dims(1) dims(2) 1])/dims(3)/voxdim(3);

kxmat = (3*(kzmat*B0unit(3)+kymat*B0unit(2)+kxmat*B0unit(1)).^2./...
    (kxmat.^2+kymat.^2+kzmat.^2)-1);

clear kymat;clear kzmat;
suscep=fftn(suscep);
suscep=-1/3*kxmat.*suscep;
clear kxmat
suscep(1,1,1)=0;
fieldshift=real(ifftn(suscep));
```

Diffusion

```
close all
clear all

tic

space_size=256;  % size of the space
spheres=zeros(space_size,space_size,space_size);
rad=14;  % perturber radius
rad2=rad^2;
nsphere=160;  % number of spheres in space
dims=size(spheres);
%% fill in spheres (can overlap)

NX = single(dims(1));  % size of the space
NY = single(dims(2));
NZ = single(dims(3));

kx=(-NX/2:NX/2-1);
ky=(-NY/2:NY/2-1);
kz=(-NZ/2:NZ/2-1);
kxmat=(repmat(reshape(kx,[NX 1 1]),[1 NY NZ]));
kymat=(repmat(reshape(ky,[1 NY 1]),[NX 1 NZ]));
kzmat=(repmat(reshape(kz,[1 1 NZ]),[NX NY 1]));

chi_array=[0.5e-7, 1.0e-7, 1.5e-7]; %susceptibility array
num_itt=length(chi_array); %looks at how many chi values there are

sigs=zeros(251, 3);
sigs0=zeros(251,3);
itt=1;


for itt=1:num_itt

%field parameters
B0=7;
gam=267.5e6;
chi=chi_array(itt);  % susceptibility
dw=B0*gam*chi;

% signal parameters
TErange=0.2;  % time range in seconds
nt=250;
TE=[0:nt]*TErange/nt;  %time over which signal evolves
dTE=TE(2)-TE(1); %time step
nt=nt+1;
dwdt=dw*dTE;

nc=0; % count number of particles

TVF=0;

nrepeat=80; %repeat this over several arrangements
rep=1;
```

```
for rep= 1:nrepeat


spheres=0;
tspheres=spheres;

for i =1:nsphere
xoff=rand(1)*(NX-1)-NX/2;  % random position of sphere centre
yoff=rand(1)*(NY-1)-NY/2;
zoff=rand(1)*(NZ-1)-NZ/2;
r2 = ((kxmat+xoff).^2+(kymat+yoff).^2+(kzmat+zoff).^2);
tspheres = (r2<=rad2);  % ones added inside sphere
spheres=spheres+tspheres;
end

SV=sum(sum(sum(spheres)));
VF=SV/space_size^3;
TVF=TVF+VF; % keep track of average volume fraction of spheres

%% field calc
voxdim=[1 1 1];
B0unit=[0 0 1];
field_map=isofieldcalc(spheres,voxdim,B0unit);


mask=1-(spheres>0);
av_off=sum(sum(sum(mask.*field_map)))/(space_size^3-SV);
field_map=field_map-av_off;  % sets average field outside spheres to zero

field_map=field_map*dwdt;   %gamma dela T *field

%tic
NP=10000;  % number of water molecules (particles)
sig=zeros(nt,1); % zero signal array
sigo=sig;

for i =1:NP

    % seed particle start position %
XC=randi(NX,1);
YC=randi(NY,1);
ZC=randi(NZ,1);


i_t=1; %timestep counter
phase=0; %set the starting point for the phase
```

```
if (mask(XC,YC,ZC)==1)  %check that particle not in a perturber

   nc=nc+1;    %only count particles for which  you generate signal
   sig(1)=sig(1)+1; %sets the signal at start time
   bz=field_map(XC,YC,ZC); %Calculates field at point (XC, YC, ZC)
   pg(i)=bz*(nt-1); %stores phase of particles if they wernt moving
   sigo=sigo+exp(1i*bz*TE'/dTE); %signal if the particles wernt moving

   tj=6; %jump size.
   rw=tj*(2*randi([0 1],3,nt-1)-1); %random step in each dimention

   rx=squeeze(rw(1,:));
   ry=squeeze(rw(2,:));
   rz=squeeze(rw(3,:));

    for i_t=1:nt-1

    new_x=mod(XC+rx(i_t)-1, NX)+1; %wraps around if it jumps out of the space
    new_y=mod(YC+ry(i_t)-1, NY)+1;
    new_z=mod(ZC+rz(i_t)-1, NZ) +1;

    if (new_x<=0)   %wraps around if it goes the other way
        new_x=NX+new_x;
    end

    if (new_y<=0)
        new_y=NY+new_y;
    end

    if(new_z<=0)
        new_z=NZ+new_z;
    end

    if mask(new_x, new_y, new_z)==1  %checks that it is not in a perturber

        XC=new_x;
        YC=new_y;
        ZC=new_z;
    end

    phase=phase+field_map(XC,YC,ZC); %adds gamma b0 at each position
    sig(i_t+1)=sig(i_t+1)+exp(1i*phase); % add in the signal

    end
    pp(nc)=phase; %this is the total phase
    end

end

rep=rep+1;
end

%toc

VF=TVF/nrepeat;
sigs(:,itt)=sig/nc;  %normalise signal by number of particles
sigsO(:,itt)=sigo/nc;

itt=itt+1;
end
```

```
label1=num2str(chi_array(1));
label2=num2str(chi_array(2));
label3=num2str(chi_array(3));

figure('Name', 'absolute signal')
plot(TE, abs(sigs(:,1)))
hold on
plot(TE, abs(sigs(:,2)))
hold on
plot(TE, abs(sigs(:,3)))
xlabel('TE')
ylabel('abs signal')
legend(label1, label2, label3)
ax.YAxis.Exponent = 0;
hold on

figure ('Name', 'Sigo')
plot(TE, abs(sigsO(:,1)))
hold on
plot(TE, abs(sigsO(:,2)))
hold on
plot(TE, abs(sigsO(:,3)))
xlabel ('TE')
ylabel('abs sigo')
legend(label1, label2, label3)
ax.YAxis.Exponent = 0;
hold on

 figure ('Name', 'Phase')
 plot(TE,angle(sigs(:,1)))
 hold on
 plot (TE, angle(sigs(:,2)))
 hold on
 plot (TE, angle(sigs(:,3)))
 legend(label1, label2, label3)
 xlabel('TE')
 ylabel('Phase')
 ax.YAxis.Exponent = 0;
 hold on

 figure ('Name', 'PhaseO')
 plot(TE, angle(sigsO(:,1)))
 hold on
 plot(TE, angle(sigsO(:,2)))
 hold on
 plot( TE, angle(sigsO(:,3)))
 legend(label1, label2, label3)
 xlabel('TE')
 ylabel('Phase')
 ax.YAxis.Exponent = 0;
 hold on

 gs1=diff(log(abs(sigs(:,1))))/dw/TVF/dTE;
 gs2=diff(log(abs(sigs(:,2))))/dw/TVF/dTE;
 gs3=diff(log(abs(sigs(:,3))))/dw/TVF/dTE;
```

```
figure ('Name', 'Gradient of ln(abs_sig)')
plot(TE(2:end),gs1, '-') % gradient of the log_e of the abs signal
hold on
plot(TE(2:end), gs2)
hold on
plot(TE(2:end), gs3)
xlabel('TE')
ylabel('Gradient of ln(abs_sig)')
hold on

gp1=diff((angle(sigs(:,1))))/dw/TVF/dTE;
gp2=diff((angle(sigs(:,2))))/dw/TVF/dTE;
gp3=diff((angle(sigs(:,3))))/dw/TVF/dTE;

figure ('Name', 'gradient of phase')
plot(TE(2:end),gp1, '-') % gradient of the phase of the signal
hold on
plot(TE(2:end),gp2)
hold on
plot(TE(2:end),gs3)
xlabel('TE')
ylabel('gradient of the phase of the signal')
hold on

figure('Name', 'stat phase');
histogram(pp) %stat phase
alpha(0.3)
hold on
histogram(pq) %stat signal
alpha(0.3)
legend('Stat phase', 'Stat Signal')

gradphase(1)=mean(gp1);
gradphase(2)=mean(gp2);
gradphase(3)=mean(gp3);

gradsigs(1)=mean(gs1);
gradsigs(2)=mean(gs2);
gradsigs(3)=mean(gs3);

gvals=gam*chi_array*B0;

figure('Name', 'Yabs comparisons') %graph for comparaison to previous data
plot(gvals, gradphase,'o')
hold on
plot (gvals, gradphase)
hold on
plot(gvals, gradsigs, 'o')
hold on
plot(gvals, gradsigs)
legend('gradphase','line', 'gradsig', 'line')
xlabel('gamma*chi*B0')
ylabel('a.u')

delg=polyfit(gvals,gradphase, 1); %makes best fit line
delp=polyfit(gvals, gradsigs, 1);
mag_slope_const=delg(1);
acc_mag_slope=mag_slope_const/0.403; %yabs value is 0.403
phase_slope_const=delp(1;
acc_phase_slope=-phase_slope_const/0.0553;

toc
```

```
Echo_T=TE.';
sigs1=abs(sigs(:,1));
phase1=angle(sigs(:,1));
sigs2=abs(sigs(:,2));
phase2=angle(sigs(:,2));
sigs3=abs(sigs(:,3));
phase3=angle(sigs(:,3));
sigtable=table(Echo_T, sigs1, phase1, sigs2, phase2, sigs3, phase3);
writetable(sigtable, 'graphfix.xlsx')
```

6.2. Appendix 2

	Diff step (n_D) (a.u)			
	2	**4**	**6**	**8**
X ($x10^{-7}$ $m^2 \cdot kg^{-1}$)	**R_2*** ($x10^{-2}s^{-1}$)			
0.50	-186.12(±0.50)	-74.08(±0.11)	-41.97(±0.09)	-25.53(±0.02)
1.00	-668.90(±2.66)	-244.81(±0.38)	-154.40(±0.23)	-91.02(±0.06)
1.50	-1016.74(±1.67)	-597.59(±1.27)	-270.01(±0.44)	-163.38(±0.13)

Table 2. Relaxation rates for three different susceptibility values at different diffusion steps.